DRAFT V-6

Design, Performance, and Calibration of CMS Hadron-Barrel Calorimeter Wedges

CMS HCAL Collaboration

Preprint submitted to Elsevier Science *15 October 2005*

Abstract

Extensive measurements have been made with beams of pions, electrons and muons on four production barrel wedges of the CMS hadron calorimeter. Data were taken both with and without a prototype electromagnetic lead tungstate crystal calorimeter module in front of the hadron calorimeter. A total of 10^8 events was taken in the H2 test beam at CERN with particle momenta varying from 20 to 300 GeV. The time structure of the events was measured with the full chain of preproduction electronics running at 34 MHz and independently with a photo-multiplier and digital scope which recorded the calorimeter pulse in 0.4 ns steps. Moving-wire radioactive source data were taken for all scintillator layers (4896 tiles). The measurements will be used to set the absolute calibration of the barrel hadron calorimeter prior to first pp collisions to approximately 2%.

Contents

1	Introduction	5
2	HCAL Barrel Wedge Design	6
2.1	Absorber Geometry	6
2.2	Scintillator	8
2.3	Longitudinal Segmentation	12
3	Test Beam Setup	13
3.1	ECAL Module	14
3.2	Trigger scintillators and wire chambers	15
4	Data Sets	15
5	Electronics and Data Acquisition	16
5.1	Front End	17
5.2	Trigger and Readout Modules	18
5.3	Data Concentrator	20
6	Determination of Layer-0 Weight	23
7	Noise Performance	24
8	Time Structure	24
8.1	QIE Measurements	26
8.2	Measurements with a Photomultiplier	28
9	HCAL Response to Beam	29
9.1	Muons	30
9.2	Pions	31
9.3	Electrons	33
9.4	Cerenkov Studies	34
10	Performance with Electromagnetic Crystals	36

10.1 Crystal Calibration 37

10.2 ECAL linearity and resolution 38

10.3 ECAL and HCAL combined performance 39

10.4 Resolution and linearity 41

10.5 Comparison with Geant4 43

11 Radioactive Source Calibration 48

12 Acknowledgments 50

References 50

1 Introduction

The Compact Muon Solenoid (CMS) [1] is designed to study pp collisions at the Large Hadron Collider (LHC) [2] with a design luminosity of 10^{34} cm^{-2}s^{-1}. The hadron calorimeter (HCAL) [3] plays a fundamental role in most anticipated LHC physics through its role in generation of level-1 trigger primitives [4], the high level trigger [5], and offline reconstruction of jets and missing transverse energy (JetMET) [6].

The design of the CMS detector starts with the 4 T solenoidal magnet of length 13 m and inner diameter 5.9 m. The magnet determines many of the features of the CMS calorimeters, since the CMS calorimeter is located inside the magnet. Figure 1 shows a quarter slice of the CMS up to the coil. The electromagnetic calorimeter (ECAL) consists of lead tungstate (PbW04) crystals. The hadron calorimeter surrounds ECAL. An important requirement of HCAL is to minimize the non-Gaussian tails of the energy resolution function. Hence, HCAL design maximizes as much interaction length of material inside the magnetic coil as possible with an additional layer of scintillators, referred to as the hadron outer (HO) detector, placed outside the coil. Copper absorber satisfies this requirement, as well as being non-magnetic. In addition, copper is fairly low Z, so it does not degrade the muon momentum measurement. Maximizing the amount of absorber before the magnet requires minimizing the amount of space devoted to active medium. The tile/fiber technology is an ideal choice. It consists of plastic scintillator tiles read out with embedded wave length shifting (WLS) fibers. This technology was first developed by the UA1 collaboration [7] and at Protvino [8] and has been used in an upgrade of the CDF endcap calorimeter [9]. It enables HCAL to be easily built with a tower geometry readout, with no uninstrumented cracks.

The HCAL contains 9072 readout channels organized into four subsystems: barrel (HB, 2592 ch.), endcap (HE, 2592 ch.), outer (HO, 2160 ch.) and forward (HF, 1728 ch.). This paper addresses the design, performance, and calibration of the HB. The performance of HE, HO, and HF were studied during a separate period under different conditions and will be reported elsewhere [10]. The HB detector is located inside the magnet coil as indicated in Fig. 1.

While beam tests of the HCAL prototype [11] and bench tests of the conceptual design of HCAL calibration [12] were reported previously, this paper reports the first measurements of production modules with the complete electronics chain. After these measurements were taken, the modules were assembled into the final barrel configuration at the LHC Point 5 surface hall (SX5) as shown in Fig. 2. One of the major goals of this work was to relate the radioactive source measurements to beam measurements in order to perform *in situ* calibration of HCAL over the lifetime of the experiment and to calibrate

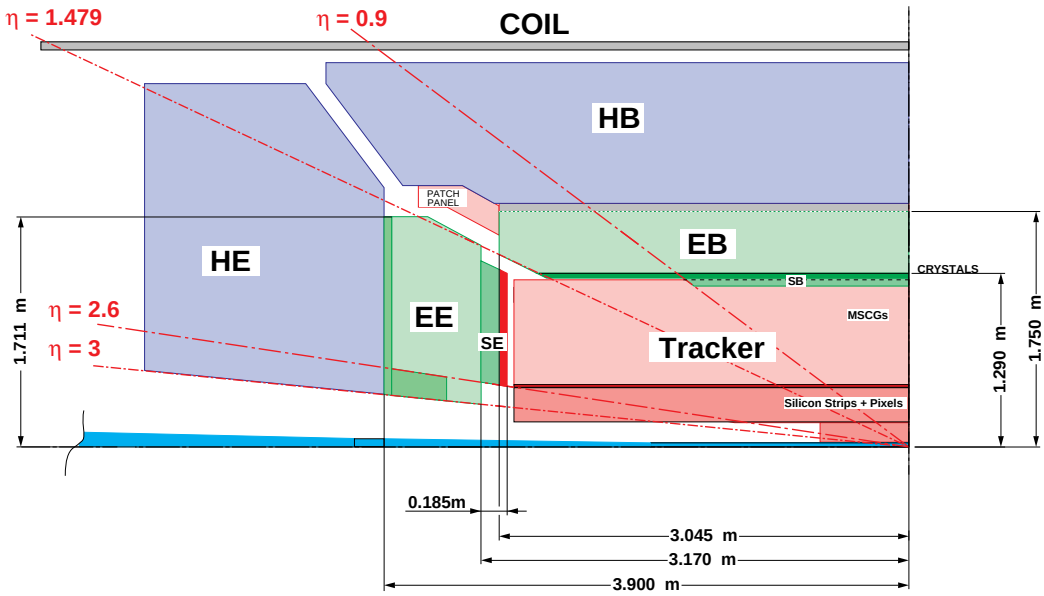

Fig. 1. Location of the HB detector inside the magnet coil.

sectors of HCAL which were not exposed to particle beams.

2 HCAL Barrel Wedge Design

The HB is a sampling calorimeter covering the pseudorapidity range $-1.3 < \eta < 1.3$ (see Fig. 1). The HB is divided into two half-barrel sections (Fig. 2), each half-section being inserted from either end of the barrel cryostat of the superconducting solenoid hung from rails in the median plane. Since the HB is very rigid compared to the cryostat, a spring mounting system is used to ensure that the barrel load is distributed evenly along the rails [3].

2.1 Absorber Geometry

The HB consists of 36 identical azimuthal wedges which form two half-barrels (HB+ and HB–). The wedges are constructed out of flat brass absorber plates (Table 1) aligned parallel to the beam axis. The numbering scheme of the wedges is shown in Fig. 3. The CMS coordinates are defined so that the positive x direction is toward the center of the LHC ring, positive y is upward and positive z is in the direction $x \times y$ Each wedge is segmented into four azimuthal angle (ϕ) sectors. The plates are bolted together in a staggered geometry resulting in a configuration that contains no projective dead material for the full radial extent of a wedge (see Fig. 4). The innermost and outermost plates are

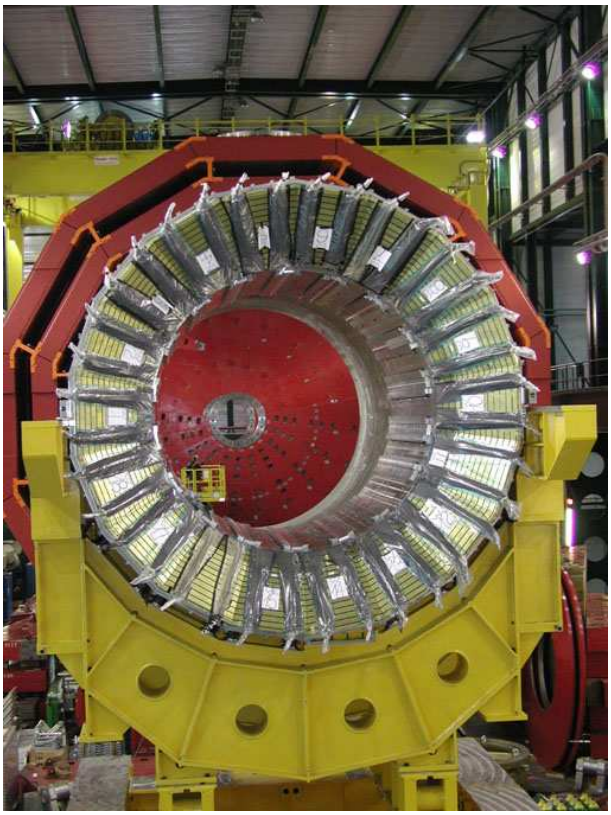

Fig. 2. Assembled HCAL half-barrel in SX5.

made of stainless steel for structural strength. The plastic scintillator is divided into 16 η sectors, resulting in a segmentation $(\Delta\eta, \Delta\phi) = (0.087, 0.087)$. The wedges are bolted together, minimizing the crack between the wedges to less than 2 mm.

The absorber (Table 2) consists of a 40 mm thick front steel plate plate, followed by eight 50.5 mm thick brass plates, six 56.5 mm thick brass plates, and a 75 mm thick steel back plate. The total absorber thickness at 90° is 5.82 absorption lengths (λ). The HB effective thickness increases with polar angle (θ) as $1/\sin\theta$, resulting in 10.3 λ at $\eta = 1.3$. The electromagnetic crystal calorimeter [13] in front of HB adds about 1.1 λ of material.

Table 1
Physical properties of the HB brass absorber, known as C26000/cartridge brass.

chemical composition	70% Cu, 30% Zn
density	8.53 g/cm^3
radiation length	1.49 cm
interaction length	16.42 cm

Table 2
Absorber thickness in the HB wedges.

layer	*material*	*thickness*
front plate	steel	40 mm
1-8	brass	50.5 mm
9-14	brass	56.5 mm
back plate	steel	75 mm

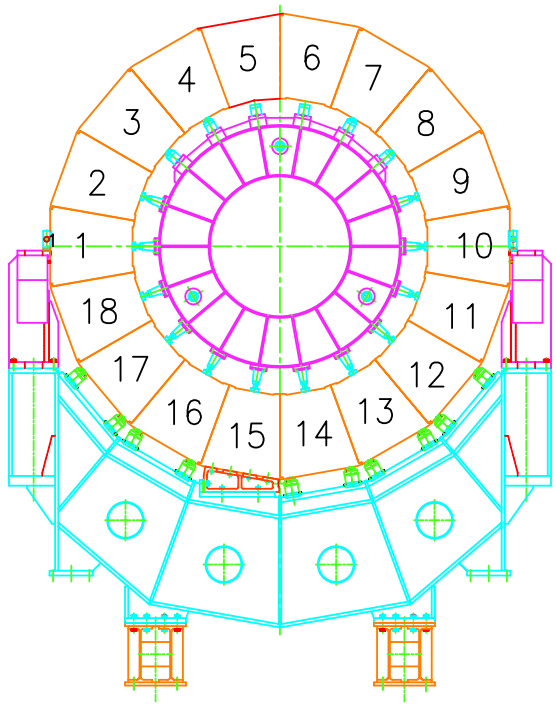

Fig. 3. Numbering scheme for the HB wedges. Wedge 1 (10) is on the inside (outside) of the LHC ring.

2.2 Scintillator

The active medium uses the tile and fiber concept as used for the CDF endcap upgrade. The CMS hadron calorimeter consists of about 70,000 tiles. In order to limit the number of individual elements, the tiles of a given phi layer are grouped into a single mechanical scintillator tray unit. Figure 6 shows a typical

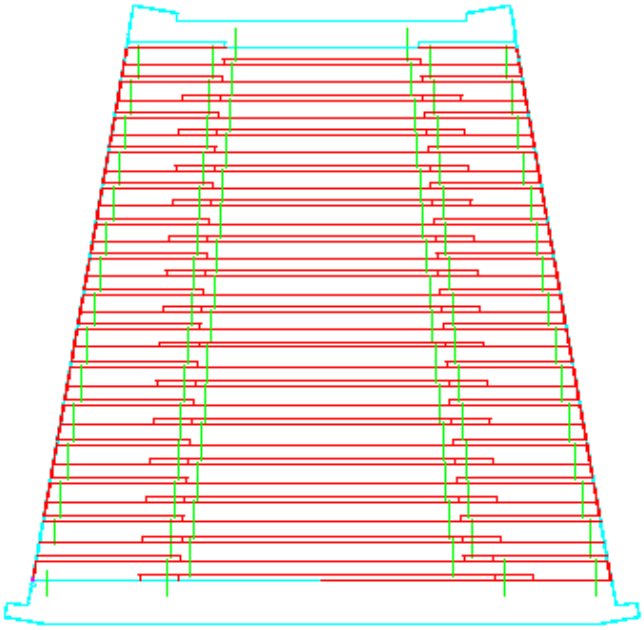

Fig. 4. Geometry of the HB wedges (r, ϕ) view.

Fig. 5. Geometry of the HB wedges (r, z) view.

tray. The tray geometry has allowed construction and testing of the scintillators remote from the experimental installation area. Furthermore, individual scintillator trays may be replaced without disassembly of the absorber in the event of catastrophic damage. Trays with segmentation of $(\eta, \phi) = (16, 2)$ go into the center of a wedge while trays with segmentation $(\eta, \phi) = (16, 1)$ go into the edge slots in a wedge (see Fig. 4). Each layer has 108 trays. Figure 7 shows a cross section of the tray.

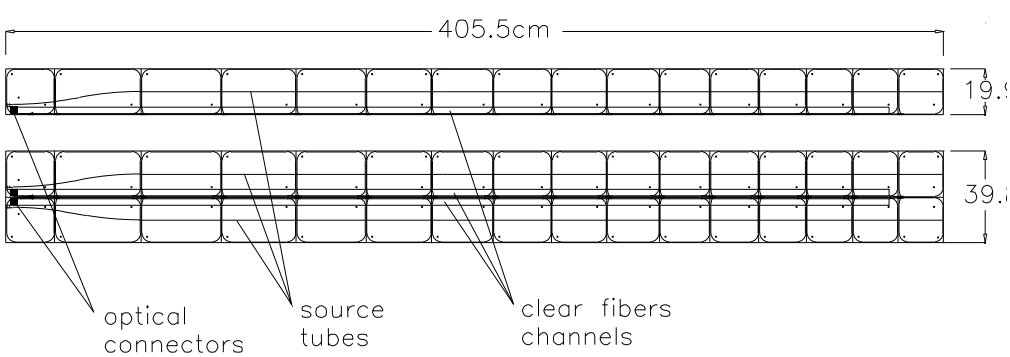

Fig. 6. Scintillator trays.

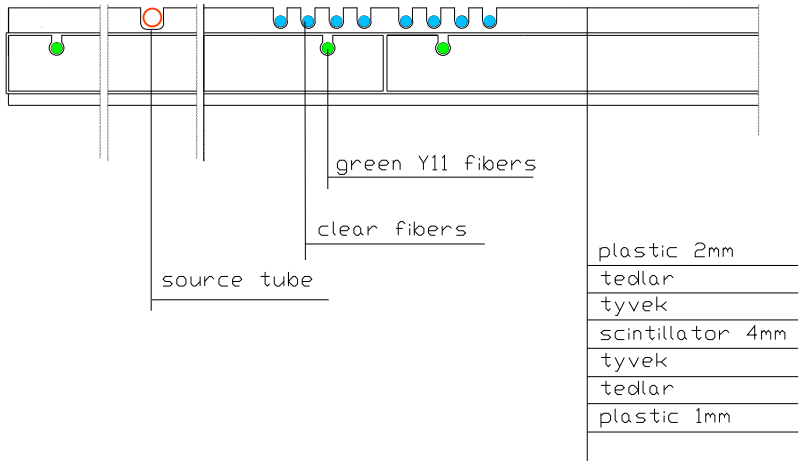

Fig. 7. Cross-sectional view of a scintillator tray.

The HB baseline active material is 4 mm thick Kuraray SCSN81 plastic scintillator, chosen for its long-term stability and moderate radiation hardness. The first layer of scintillator (layer 0) is located in front of the steel support plate. It was originally foreseen to have a separate readout [3] and is made of 9 mm thick Bicron BC408.

Table 2. Scintillator in the HB wedges.

layer	*material*	*thickness*
0	Bicron BC408	9 mm
1-15	Kuraray SCSN81	3.7 mm
16	Kuraray SCSN81	9 mm

A tray is made of individual scintillators with edges painted white and wrapped in Tyvek 1073D which are attached to a 0.5 mm thick plastic substrate with plastic rivets. Light from each tile is collected with a green double-cladded wavelength-shifting fiber (Kuraray Y-11) placed in a machined groove in the scintillator. For calibration purposes, each tray has 1 mm diameter stainless steel tubes, called "source tubes," that carry Cs137 radioactive sources through the center of each tile. An additional fiber is used to inject laser light into the tiles. The top of the tray is covered with 2 mm thick white polystyrene. The cover is grooved to provide routing for fibers to the outside of the tray and also to accommodate tubes for moving radioactive sources.

After exiting the scintillator, the wavelength shifting fibers are spliced to clear fibers (Kuraray double clad). The clear fiber goes to an optical connector at the end of the tray. An optical cable takes the light to an optical descrambler. The descrambler arranges the fibers into readout towers and brings the light to a hybrid photomultiplier tube (HPD) [14]. An additional fiber eneters each

HPD for direct injection of light using either the laser or a light emitting diode (LED). Since the phototransducer will be operating in the 4 T magnetic field, conventional photomultipier tubes will not work. A schematic of the overall layout is shown in Fig. 8 and the actual cabling is shown in Fig. 9.

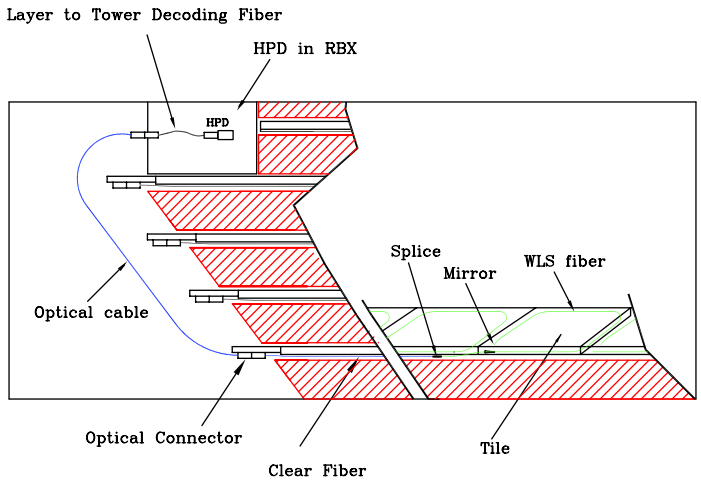

Fig. 8. Schematic of the HB optics.

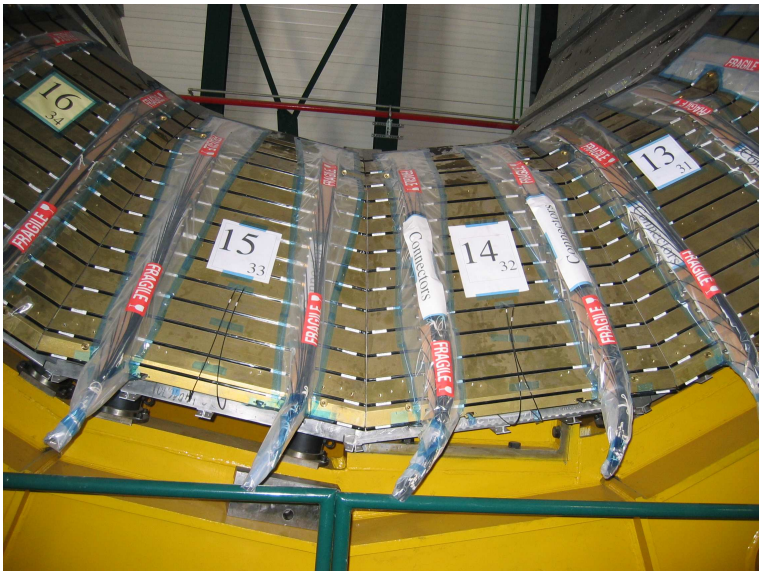

Fig. 9. Close up view of the assembled HB wedges, showing the optical cabling.

During the production and assembly process, the WLS fibers are cut, polished, and mirrored. The reflectivity of the mirror is checked by measuring test fibers which are mirrored along with the fibers used in the calorimeter. Measuring the reflectivity of the mirror is done with a computer controlled UV scanner with the fibers read out by pin diodes. Clear fibers are spliced onto WLS fibers with a fusion splicer. The transmission across the splice is checked by splicing

a sample of WLS fibers onto WLS fibers. The splice region is measured with the UV scanner. The transmission across the splice is 92.6% with an RMS of 1.8%. Next, the optical fibers are glued into a 10 fiber connector. This configuration is called a pigtail. In order to get the fiber lengths correct, the pigtail is assembled in a templet. The connector is diamond polished. The fibers are measured with the UV scanner. The scanner checks the green fiber, clear fiber, splice, and mirror. The RMS of the light from the fibers is 1.9%. After the pigtail is inserted into the tray, the completed tray is checked with an automated source scanner using a Cs137 source inside a lead collimator. This yields a 4 cm diameter source spot on the tray. The collimator is moved with a computer controlled x-y motor. From the scanner we determine the relative light yield of each tile and the uniformity of the each tray. The gain of the individual tiles has an RMS of 4.6%, while the transverse uniformity of the megatile is 4.5%. A Cs137 wire source is run through the 3 source tubes and the light yield is measured. The RMS of the ratio of collimated source to wire source is 1.3%. This means the line sources, which can be used when the calorimeter is completely assembled, can calibrate the tiles to better than 1.3%.

The wedges have several methods to monitor the calibration. In addition to the moving wire source, there are laser and LED light injection systems. The HPD that reads out the calorimeter has an additional fiber going to it. Either the laser or LED can inject light into this fiber. As shown on the drawing of the megatile, there is a fiber which can also inject light into a tile.

2.3 Longitudinal Segmentation

The η towers 1-14 have a single longitudinal readout. The η towers closest to the end cap transition region (15 and 16) are segmented in depth. The front segment of tower 15 contains either 12 or 13 scintillators, due to the placement of the readout box and the staggering of the layers (layers 0-11 for the middle two phi sectors and 0-12 layers for the outer two phi sectors). The rear segment of tower 15 has three scintillators. Tower 16, which is in front of the endcap (HE) has five scintillators in the front segment and three in the rear. The front segment of tower 16 does not have a layer-0 scintillator. This tower segmentation is summarized in Fig. 10.

Table 3. Tower configuration of HB.

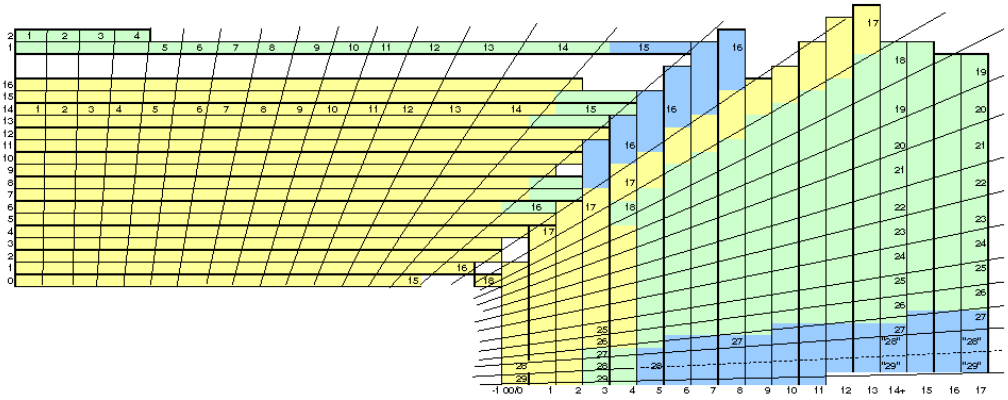

Fig. 10. The HCAL tower segmentation in the r, z plane for one-fourth of the HB, H) and HE detectors. The numbers on the left (0-16) indicate the scintillator layers. The shades represent different longitudinal readouts.

tower	*eta range*	*thickness* (λ)
1	0.000 - 0.087	
2	0.087 - 0.174	
3	0.174 - 0.261	
4	0.261 - 0.348	
5	0.348 - 0.435	
6	0.435 - 0.522	
7	0.522 - 0.609	
8	0.609 - 0.696	
9	0.696 - 0.783	
10	0.783 - 0.870	
11	0.870 - 0.957	
12	0.957 - 1.044	
13	1.044 - 1.131	
14	1.131 - 1.218	
15	1.218 - 1.305	
16	1.305 - 1.392	

3 Test Beam Setup

The data were recorded during 2002 at the CERN H2 test beam. A moving platform held two production HB wedges plus a prototype electromagnetic

crystal calorimeter which was inserted for some of the measurements (see Fig. 11). The two-dimensional movement of the platform allowed the beam to directed onto any impact point on the calorimeter in (η, ϕ) space. The beam line was equipped with four 1 cm thick scintillator counters for triggering and two sets of wire chambers to monitor the beam transverse (x, y) position and incident direction, event-by-event.

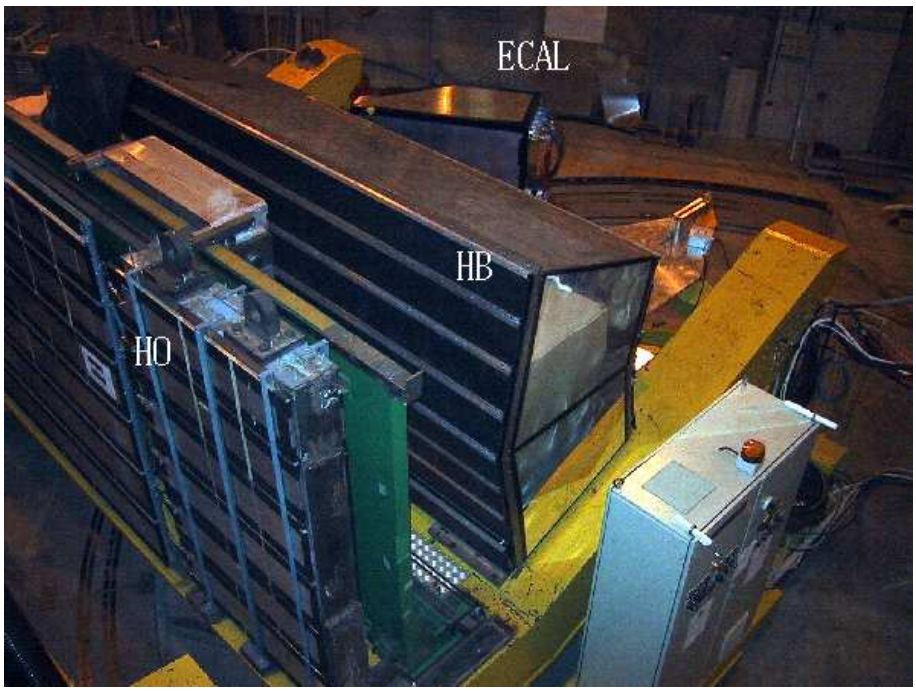

Fig. 11. Two HB wedges (144 tiles) and the prototype electromagnetic (7×7) crystal calorimeter module mounted on the moving platform.

The range of motion of the rotating platform was limited to $1 < \phi < 6$ (all four phi sectors in the bottom wedge and the bottom two phi sectors in the top wedge. The position of the platform was measured electronically and recorded in the data stream. The detector response provided an accurate calibration of the detector position with respect to the beam. This is discussed further in Section 9.

3.1 ECAL Module

The electromagnetic calorimeter module used for the combined calorimeter measurements consisted of 49 lead tungstate crystals, each of size 2.2×2.2×23 cm^3, arranged in a 7x7 block. The crystals are tapered so that they have a slightly smaller upstream cross section. On the end of each crystal, a plastic light guide sent the light produced in the crystals to 49 separate photomultiplier tubes (Hamamatsu R7524). The light guides are located on the front

end of the crystals as seen in Fig. 12. Not shown in the diagram is the 12.3 cm between the end of the crystals and the end of the box. The space includes a 7 mm aluminum plate that holds the crystals in place. There is also an aluminum block which corresponds to approximately the same amount of material and same atomic number that will exist in CMS between the crystals and the HCAL. The distance between the fixation point and the aluminum block is 10.5 mm. The PMT signals were converted to ADC counts using V972 charge-to-digital converters (QDC). Five thermocouples were distributed inside of the aluminum box for temperature monitoring.

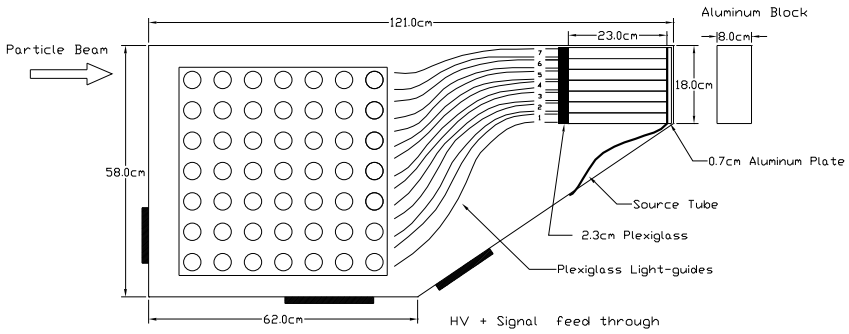

Fig. 12. Schematic drawing of the electromagnetic calorimeter module, top view.

3.2 Trigger scintillators and wire chambers

Four scintillation counters of size 14×14, 4×4, 2×2, and 14×14 cm^2 were located approximately three meters upstream the ECAL module. A coincidence between the 2×2 and one of the 14×14 counters was used for the trigger. Since the crystal transverse size was larger than the trigger area, if one of the ECAL crystals was centered on the beamline, all triggered events should have particles hitting the chosen crystal.

4 Data Sets

The data were recorded in the period August-October 2002. The SPS had 16.8 s duty cycle and 4.8 s extraction time; 12 seconds were used for filling SPS and acceleration. The H2 beamline received beam only during the 4.8 sec extraction time, referred to as the "spill." A total of 10^8 events were recorded in 3131 runs (53991 accelerator spills). Data were taken with electron beam momenta of 20, 30, 50 and 100 Gev/c, pion beam momenta of 20, 30, 50, 100, and 300 GeV/c, and a muon beam momentum of 225 GeV/c (see Table 3). Special runs were taken with an LED pulser and moving radioactive source.

Table 3. Summary of the beam data taken.

beam	*events* (10^6)	*momentum* (GeV/c)
electron	26	20, 30, 50, 100
pion	35	20, 30, 50, 100, 300
muon	11	225

Two sets of data were taken with HB production wedges. The first measurements were performed with wedges 5 (top) and 6 (bottom) and then repeated with wedges 4 (top) and 7 (bottom). The measurements included a complete radioactive sourcing of all 17 scintillator layers in each phi sector (2448 tiles). Beams of muons, pions and electrons were directed into the centers of all towers we could reach with the moving table, which included all four phi sectors of wedge no. 6 but was limited to the bottom two phi sectors of wedge no. 5. For both wedges, the scan covered the entire eta range (16 sectors). These data were taken with no ECAL present.

A number of dedicated runs were taken to calibrate the 7×7 array of ECAL crystals. The calibration procedure is described in Section 10. The HCAL readout was then modified to read layer-0 separately and data were taken with ECAL and HCAL together.

The first beam data were taken with no ECAL in place. Negatively charged pions of momenta 225 GeV/c were directed into the centers of all towers that could be rotated into the beam. As each phi scan was completed with pions, it was repeated with negatively charged muons of momenta 225 GeV/c. After the π/μ scan was completed, it was repeated with 100 GeV/c positrons. For a group of selected towers in wedge 5 ($\phi = 3$ and η =3, 7, 11, 15, and 16, we did a momentum scan with negative pions (20, 50, 100, 150, 200, 250, and 300 GeV/c) and positrons (20, 50, 100, 120, and 150 GeV/c). With the ECAL in place, we then did a transverse (ϕ) scan at $\eta = 3$ and also at the boundary between $\eta = 3$ and $\eta = 4$ with negative pions of momenta 50, 100, and 300 GeV/c and positrons of 100 GeV/c. This served to explore the uniformity of the response when crossing phi sectors including the wedge boundary.

5 Electronics and Data Acquisition

Figure 13 shows an overview of the HCAL electronics and data acquisition system planned for the CMS experiment. The key elements tested during these measurements were 1) front end electronics at 34 MHz with gigabit optical link (GOL), 2) HCAL trigger and readout (HTR) cards with channel links, 3)

data concentrator (DCC) with SLINK 32, and the LHC trigger, timing and control (TTC) clock.

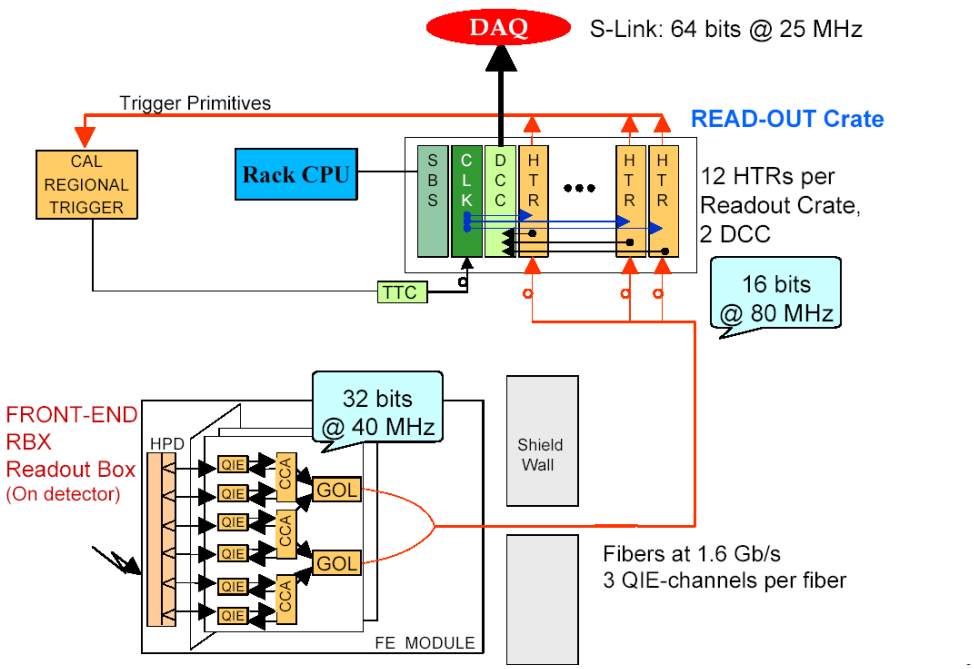

Fig. 13. Overview of the HCAL data acquisition electronics.

5.1 Front End

Each wedge has 72 channels of front end electronics mounted on the detector periphery near tower 16, loated in a readout box. Each of these readout boxes is further divided into four readout modules (RM). Each RM contains an 18 channel hybrid photodyode (HPD) [14] which collects light from towers at a fixed value of azimuthal angle (ϕ). The 18 HPD signals are sent into three 6-channel readout cards located inside the RM. The readout card is based on a custom ASIC which performs charge integration and encoding (QIE) [15]-[16]. The QIE is designed to provide approximately constant precision over a wide dynamic range. This is accomplished with a floating-point ADC in which the bin width is increased in proportion to the input amplitude. The signal is integrated on four ranges that are offset to be non-interlapping. In addition, the QIE has four time-interleaved stages so that the signal in each beam crossing period is integrated and digitized. The output of the QIE is a pseudo floating point format with 2 bits of range (exponent) and 5 bits of mantissa. The front-end card which contains six QIE chips is shown in Fig. 14.

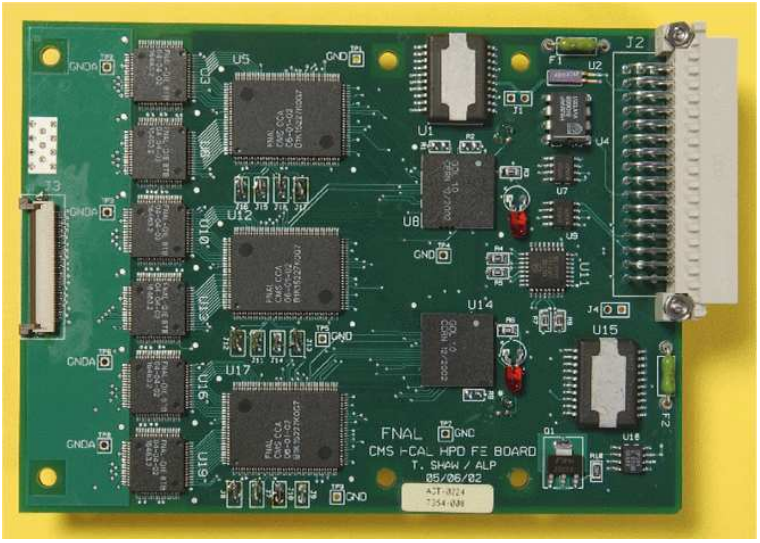

Fig. 14. Front-end electronics card (six channel) based on the QIE ASIC. The six QIE chips are on the left.

5.2 Trigger and Readout Modules

The data are sent from the detector to HCAL trigger and readout modules (HTR) via gigabit optical links (GOL). Each link carries three channels of data. The HTR cards used for these measurements were 24 channel units in a 9u VME format. A total of six HTR cards were used to read out the two wedges simultaneously (144 channels).

The HTR is a 9U VME module (Figure 15) equipped with optical receivers, TTCrx circuitry, outputs on serial LVDS (Channel Link) and a custom mezzanine card. The optical inputs receive data from the HCAL front-end electronics, with one charge sample per bunch crossing (BX). The high-speed serial inputs require special board layout techniques. The CMS HCAL is a trigger detector, thus the HTR includes two data pipelines: the trigger pipeline, which assigns Front-End data to a BX and sends them to the CMS regional trigger, and the DAQ pipeline where the FE-data are pipelined, triggered and sent to the Data Concentrator Card. For these measurements, the trigger pipeline was not used.

The design of the HTR module was based on the Xilinx XCV1000E-FG900 field programmable gate array (FPGA). A control FPGA (Altera EPF10K50VQC240-3) was used to interface the HTR to the VME bus as well as to configure the main Xilinx FPGA and store the configuration on flash memory.

The HTR input processing and level-1 data pipeline is shown in Fig. 16. The raw fiber data stream is deserialized, then synchronized to the local clock. A

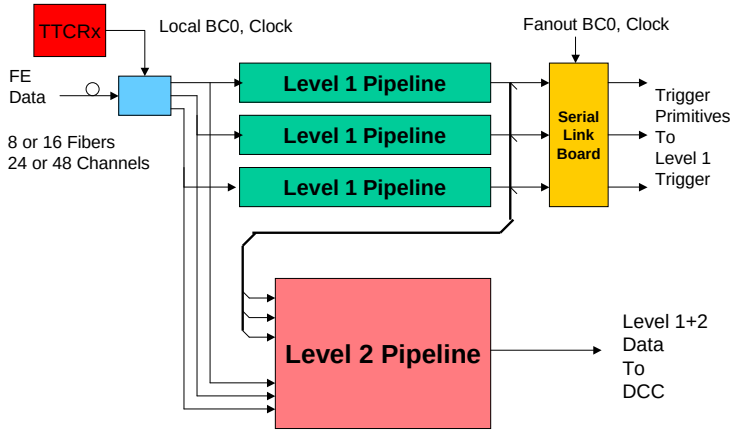

Fig. 15. Block diagram of the HTR electronics.

programmable delay of up to a few clock cycles is used to align data from different input fibers. A test RAM can substitute for the input data stream. Finally, the channels carried on one fiber are demultiplexed. Each channel is then fed to a linearizing look-up table which converts raw input data to a 16-bit linear energy value. Next a finite-impulse response (FIR) filter is used to subtract the pedestal and assign all the energy to a single bunch crossing. This performs the same function as a traditional analog shaper, but has the advange of being easily reprogrammable. Finally, the energy is converted to E_T and compressed to 8 bits according to a non-linear transformation specified by the CMS level 1 calorimeter trigger, and a comparison is done to see if the signal may represent a muon. This compressed output plus a muon ID bit is sent to level 1. The final synchronization and serial transmission is performed by a Synchronization and Link Board (SLB). The latency of the level 1 pipeline is critical; it must be less than $\approx$ 20 BX periods.

The HTR level-2 Pipeline is shown in Figure 17. First there is a pipeline of programmable depth which stores data during the CMS level 1 latency period (a fixed value). Then comes a "derandomizer" buffer into which data are copied at each level 1 accept. The derandomizer can hold up to 10 charge samples (one per BX) per event although currently we anticipate only processing 5 samples. Note that a given charge sample can in principle participate in multiple events, so the pipeline-to-derandomizer copy logic must handle overlapping events. From the derandomizer, data are linearized by a look up talbe (LUT), filtered by an FIR filter similar to that in the level 1 pipeline, and a threshold is applied for zero-supression. At this point either the output of the filter, the raw data or both may be inserted into the output data stream.

A similar pipeline is used to store the level 1 trigger primitives, synchronized with the corresponding level 2 data. Finally the data are packaged in a variable-length block format along with any error information from the input

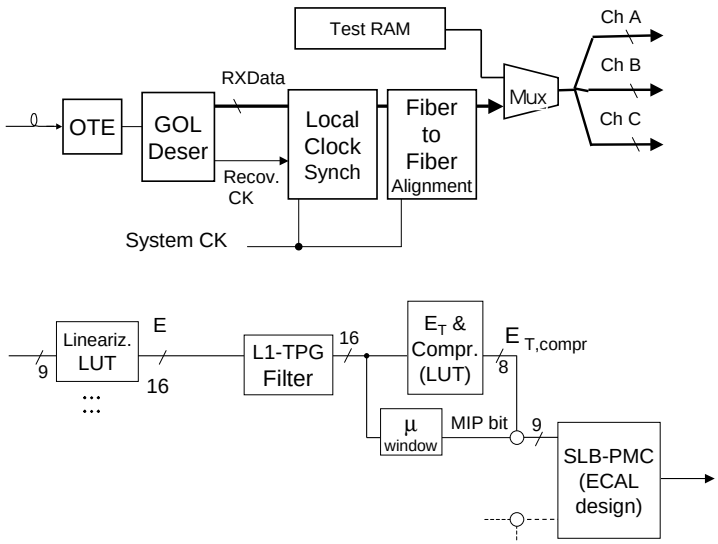

Fig. 16. Detail of the level-1 data pipeline in the HTR electronics.

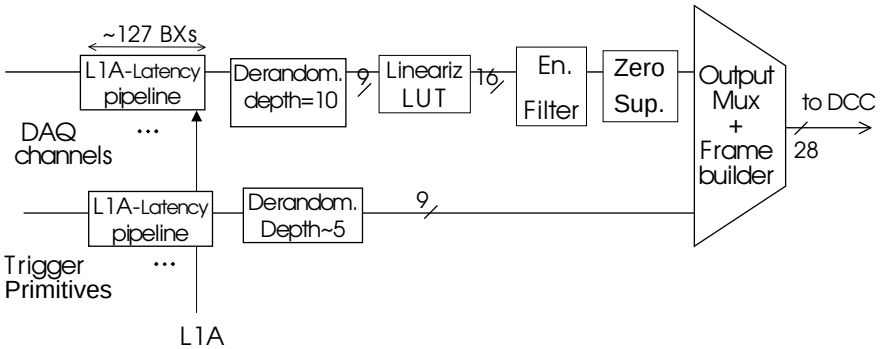

Fig. 17. Detail of the level-2 data pipeline in the HTR electronics.

links and transmitted using an LVDS serializer to the data concentrator.

5.3 Data Concentrator

The Data Concentrator Card is composed of a VME motherboard which supports up to six LVDS link receiver boards and a PMC-type logic board. The motherboard is a VME64x 9Ux400mm single-slot module. The motherboard (Fig. 18) supports VME access up to A64/D32, and contains three bridged PCI busses. Six PC-MIP mezzanine sites are arranged in groups of three on two 33MHz 32-bit PCI busses. A third 33MHz 64-bit PCI bus is bridged to the VME bus using a Tundra Universe II VME-to-PCI bridge.

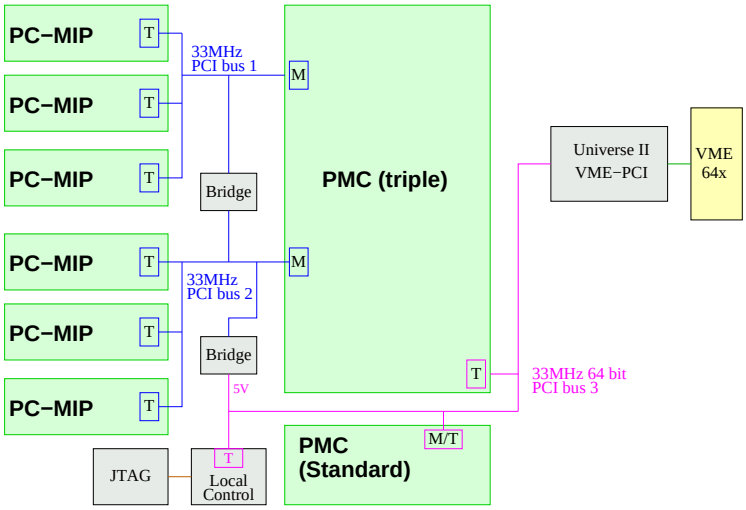

Fig. 18. Block diagram for the data concentrator motherboard.

A single large logic mezzanine board has access to all three PCI busses for high-speed application-specific processing, and an additional standard PMC site is available. A local control FPGA on the motherboard provides access to on-board flash configuration memory, a programmable multi-frequency clock generator, and JTAG.

The LVDS link receiver boards (Fig. 19) use Channel Link [17] technology from National Semiconductor. Each board contains three independent link receivers which can operate at 20–66MHz (16-bit words). Buffering for 128K 32-bit words is provided for each link with provision to discard data if buffer occupancy exceeds a programmable threshold. Event building, protocol checking, event number checking and bit error correction are performed independently for each link. A PCI target interface provides single-word and burst access to the data stream, plus numerous monitoring registers. A single PCI burst read serves to build an event from fragments found in each of the three input buffers. The expected event number (low eight bits) is provided as part of the PCI address, and a mis-match causes an error bit to be set in the link trailer.

The logic mezzanine board contains the core data concentrator logic. The prototype was implemented using a Xilinx XC2V1000 for the logic, plus three Altera EP1K30 for three PCI bus interfaces.

The event builder logic merges two data streams from the two PCI busses, and re-orders the incoming data so that the various sub-types (Level 1, Level 2...) are in contiguous blocks in the output stream. An on-board TTCrx stores level 1 accepts (L1A) into a FIFO which drives the event builder. For each L1A, the *data decoder* triggers a PCI burst read on the PCI-1 and PCI-2

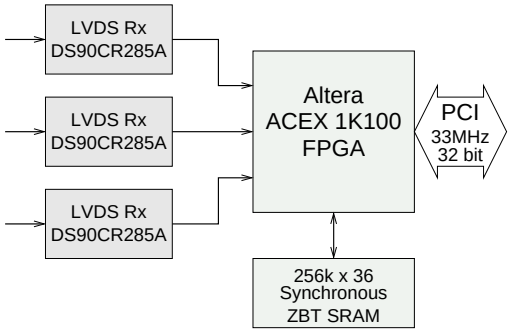

Fig. 19. Block diagram of the PC-MIP 3-Channel Link Receiver Board

interfaces simultaneously. As data are transferred they are sorted into various sub-types and summary and monitoring information is collected. Each sub-type is pushed into a unique FIFO. After the end of the event has been processed (block trailer received from LRB) an end-of-event marker is pushed into each of the FIFOs. The *event builder* reads data from each of the sub-type FIFOs in turn, inserting protocol words as needed. The DCC logic is designed to operate continuously at the full speed of the two input PCI busses, namely 33MHz∗32 bits∗2. The event builder and output logic must thus run at an average rate of at least 66MHz (32-bit words) or 264MBytes/sec.

The event builder output is sent in parallel to several destinations. Each output path contains a filter which can be programmed to select specific portions of events or a specific subset of events (prescaled, specially marked, *etc.*).

(1) The DAQ Output. Every event were sent via SLINK-32 to the CMS DAQ. The detailed contents of each event may be controlled by configuration registers.
(2) The Trigger Data Output. The trigger primitives sent to the CMS L1 trigger are also sent to via SLINK-64 to a special "trigger DAQ" system for monitoring of the trigger performance.
(3) The Spy Output. A selected subset of events is sent to a VME-accessible memory for monitoring and diagnostics.

Error detection and recovery are a primary consideration in a large synchronous system and the DCC contains logic dedicated to this purpose. Figure 20 shows the main DAQ data pipeline and buffering in the HCAL readout system. Hamming error correction is used for the LVDS links between the HTR and DCC. All single-bit errors are corrected and all double-bit errors

are detected by this technique. Event synchronization is checked by means of an event number in the header and trailer of each event, which are checked by the LRB logic against the TTC event number. Buffer overflow is avoided by the expedient of discarding the data payload and retaining only header and trailer words when the LRB buffer occupancy exceeds a programmable level. Additionally, an "overflow warning" output is provided which is delivered to the CMS trigger throttling system to request a reduction in the rate of L1A. Data transfers from the LRB to DCC logic are protected by parity checks on the PCI busses. The event builder operates at a processing speed sufficient to handle 100% occupancy of the two PCI busses. After the event builder is a large memory, which can contain several thousand average-size event. A schematic of the HCAL bufering is shown in Fig. 20. The DCC used for these measurements is shown in Fig. 21.

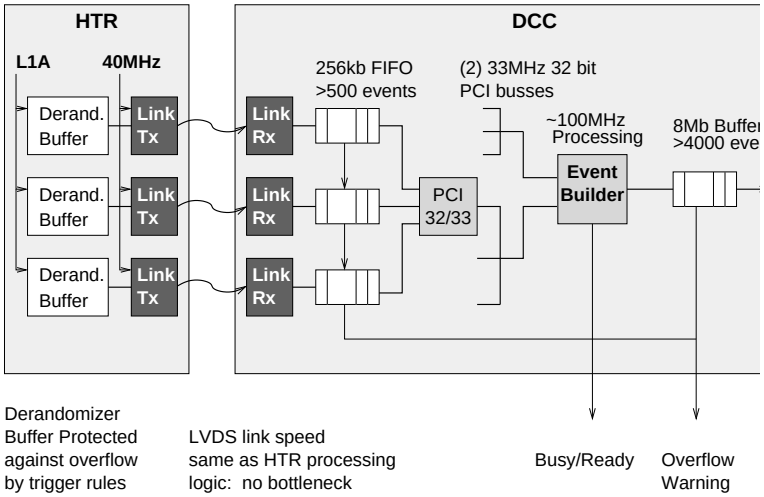

Fig. 20. HCAL DAQ Buffering

6 Determination of Layer-0 Weight

The HCAL was originally foreseen to have the possibility of a separate readout for the front layer of scintillator (layer 0). Since it was decided subsequently to eliminate separate readout of layer 0, it became necessary to determine a proper weighting factor which was implemented as an optical attenuation. At the beginning of the test beam period, we made a series of special runs with layer 0 read out separately. Offline we applied a variable weight (α) to layer 0 and performed fits to the resulting energy resolution. The best resolution was obtained with a layer 0 weight of 0.3. These data were taken with our best estimate of the material between ECAL and HCAL (8 cm of aluminum). Additional data were taken with varying amounts of material (0,2, 4, and 6 cm of aluminum) in case it should be possible to reduce it in the final

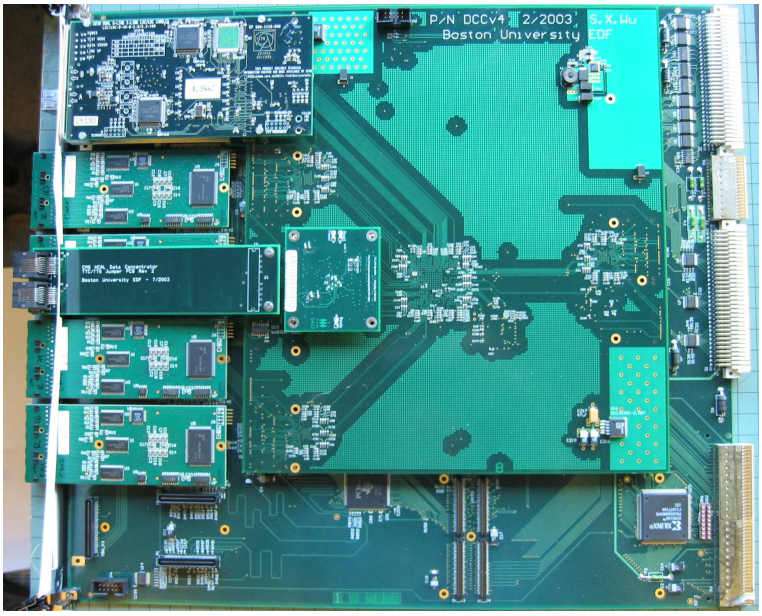

Fig. 21. Data concentrator.

configuration.

7 Noise Performance

The front end electronics was operated at 33.79 MHz for these measurements. Figure 23 shows the measured noise distribution at the highest gain setting of the multi-range ADC, for a single QIE channel. The results for the four capacitor banks (Cap 0, Cap 1, Cap 2, and Cap 3) are shown individually. One least count corresponds to a noise of about 2000 electrons, so that the observed noise (2.3 counts) less than 5000 electrons. Figure 24 shows the resulting noise for a complete readout module (18 QIE channels times 4 cap IDs). As will be seen from the beam measurements, this figure corresponds to an rms electronic noise of about 0.5 GeV,

8 Time Structure

The time structure of the HCAL calorimeer pulse is dominated by the choice of scintillator and optics. The electronics, including the choice of photo detector should be fast enough to not distort the pulse. Knowledge of the calorimeter pulse shape, *i.e.*, the time dependence of the light collection, is essential in order to identify an energy deposit with a particular beam crossing. Such

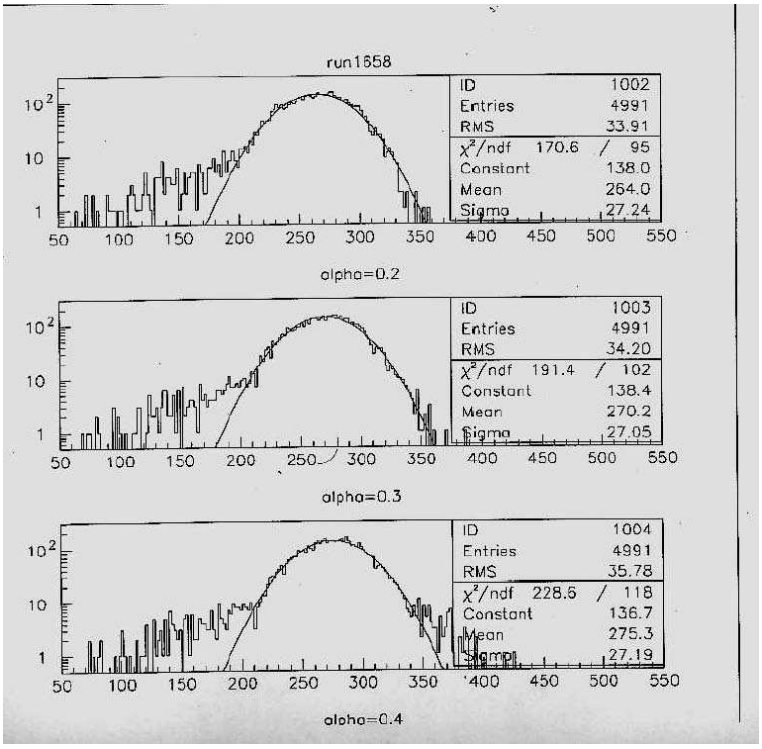

Fig. 22. Fit to the energy resolution with different weights applied to layer 0. The plots correspond to (top to bottom) a layer-0 attenuation of 0.2, 0.3, and 0.4, respectively. Note the appearance of the high-side tail at $\alpha = 0.4$.

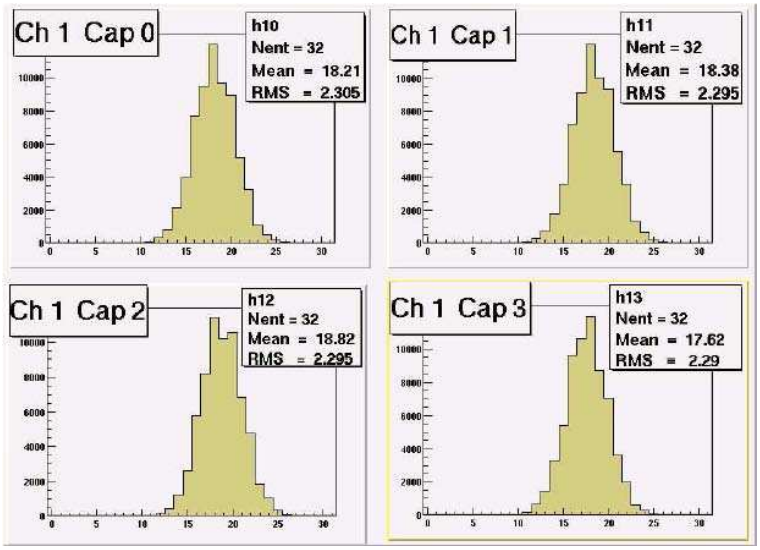

Fig. 23. Measured pedestal distributions in calibration mode. The four plots correspond to the 4 capacitor banks of the QIE. For these measurements, the QIE was running at 33.79 MHz.

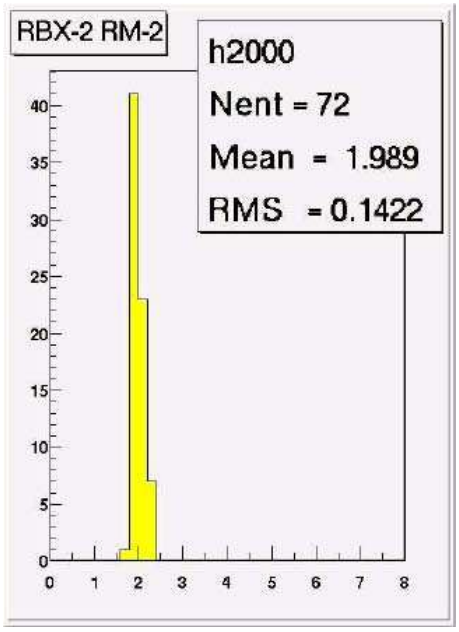

Fig. 24. Measured rms noise at the highest ADC gain, for a complete readout module (18 channels × 4 cap IDs). One count corresponds to 2080 electrons.

event synchronization is needed for generation of the level-1 calorimeter trigger primitives. We have made measurements of the calorimeter pulse shape using two different techniques. For one measurement, we read out a portion of the calorimeter light with a photomultiplier and commercial electronics. Independently, we read out the time samples with the HPD/QIE electronics.

8.1 QIE Measurements

Twenty time samples were recorded for each QIE channel. The timing was adjusted so that the event occurred near the middle of the time sequence (sample number 10) allowing to record the noise performance before and after the event. At a frequency of 33.79 MHz, each time sample corresponds to 29.6 ns (slightly longer than the 25 ns that will be used at the LHC). These data show that most of the signal is collected in two time samples. Operation of the electronics at 40 MHz, which is little changed from these measurements, will be reported elsewhere [10]. Figure 25 shows the time structure (20 samples) for eight consecutive events measured with the QIE electronics. The relative phase of each event is random, corresponding to the random occurrence of the collision within the spill.

If we select the event phase by requiring that 10-12% of the observed energy is in time sample number 10 as is shown in Fig. 26, then all the events have the same temporal shape. We have complete freedom to adjust this shape for CMS

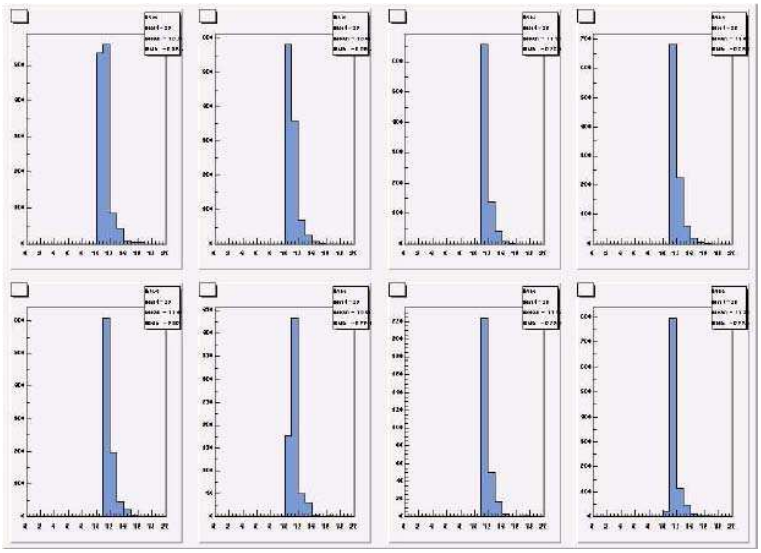

Fig. 25. Time structure for eight consecutive events. The relative event phase is random.

running. Figure 27 shows the fraction of energy in two times slices (vertical scale) vs. the fraction of energy observed in a single time slice (horizontal scale). The different points on the graph represent differt choices of the event phase. One can see that it is possible to have 75% of the energy in a single time slice and more than 90% of the energy in two time slices. The results are only slightly changed at 40 MHz [10].

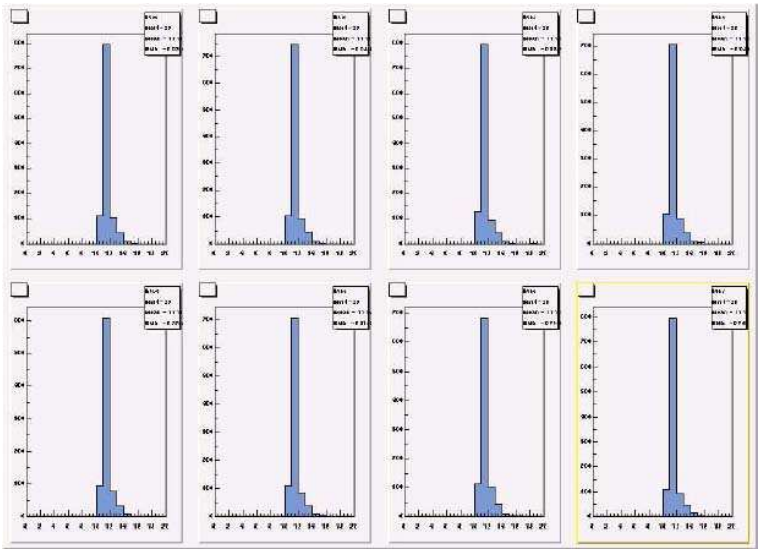

Fig. 26. Time structure for eight events in which the phase is selected by demanding that 10-12% of the observed energy is in time sample number 10.

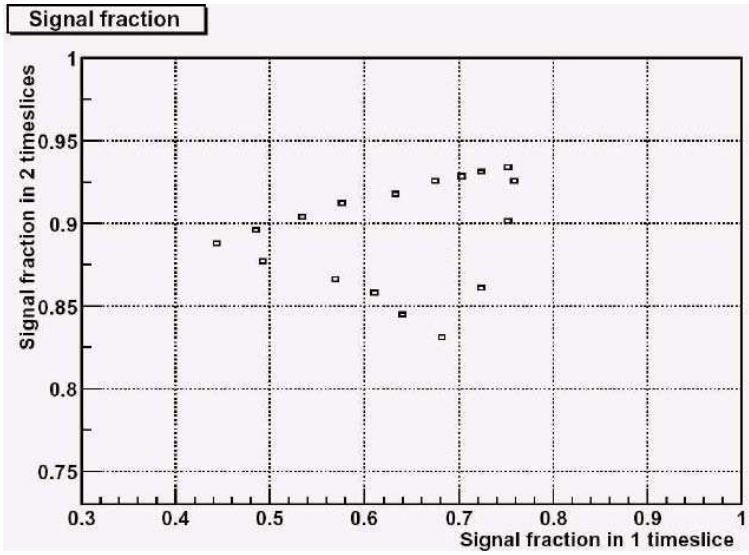

Fig. 27. Fraction of energy observed in two time slices vs. that observed in a single time slice.

8.2 Measurements with a Photomultiplier

The use of a photomultiplier allows readout of the calorimeter signal with high gain, allowing observation of the time structure of individual photoelectrons. This was accomplished during this test beam period by constructing a special optical unit that coupled the light from one 5° phi slice of a wedge (16 eta towers) into a single 10-stage, 2-inch photomultipler (RCA 6342A). The output of the photomultipler was fed into a LeCroy digital scope which recorded voltage *vs.* time in 0.4 ns steps. Events were recorded in each of four categories: a) 300 GeV pion showers, b) 20 GeV pion showers, c) 100 GeV electron showers, and d) minimum ionizing muons. Sample events are shown in Figs. 28-31..

Adding a number of minimum-ionizing muon events together, we would expect to reproduce the same pulse shape as observed in a single pion show. Figure 32 shows this to indeed be the case. The tail of the distribution is due to the optical properties of the system and not an atrifact of the phototube or electronics.

The pulse shape was observed to be very stable. Figure 33 shows the fraction of energy observed in four consecutive time bins of width 29.6 ns.

In Fig. 34 we show, from phase selected events, the average pulse shape vs. time in 29.6 ns bins. The pulse shape agrees very well with that measured with the HPD and QIE electronics, providing independent confirmation of the time structure of the calorimeter pulses.

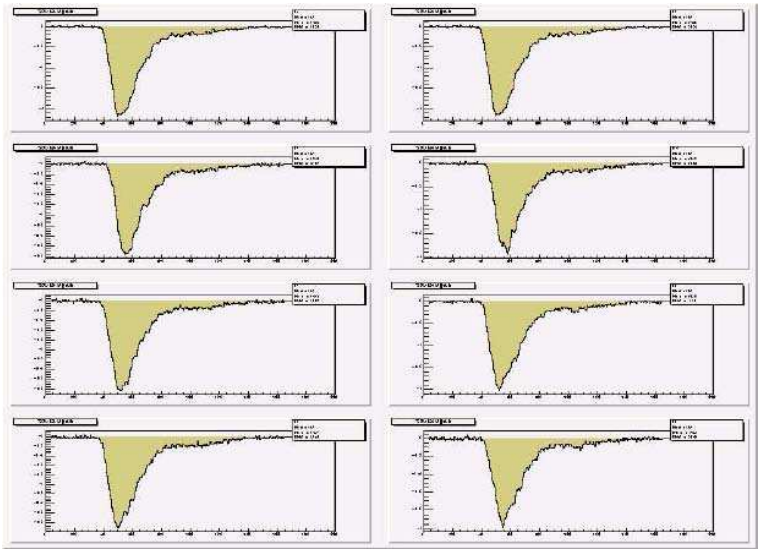

Fig. 28. Calorimeter pulses for eight individual events, voltage *vs.* time, observed with a photomultipler for 300 GeV pion showers. The time scale is 0.4 ns per bin.

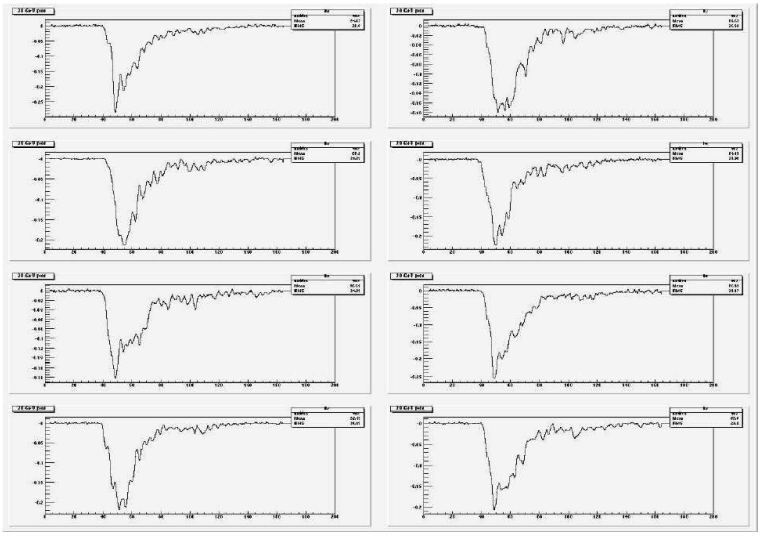

Fig. 29. Calorimeter pulses for eight individual events, voltage *vs.* time, observed with a photomultipler for 20 GeV pion showers. The time scale is 0.4 ns per bin.

9 HCAL Response to Beam

Beams of pions, electrons, and muons of various energies were sent directly into HCAL towers.

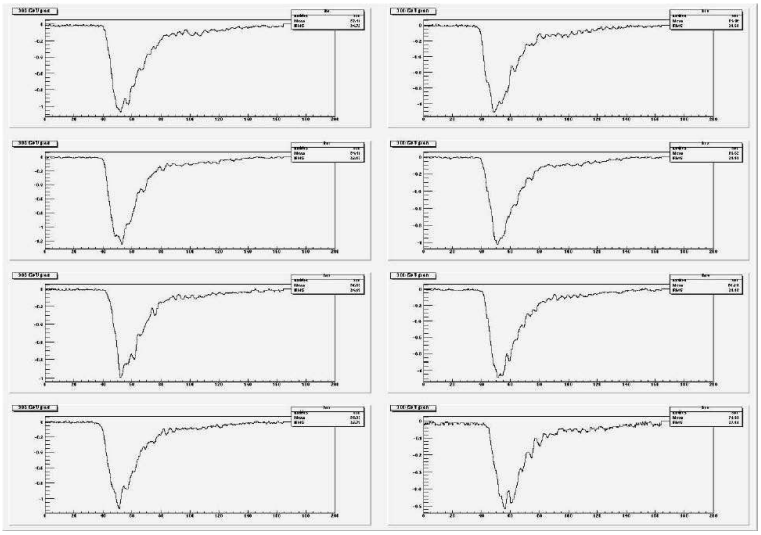

Fig. 30. Calorimeter pulses for eight individual events, voltage *vs.* time, observed with a photomultipler for 100 GeV electron showers. The time scale is 0.4 ns per bin.

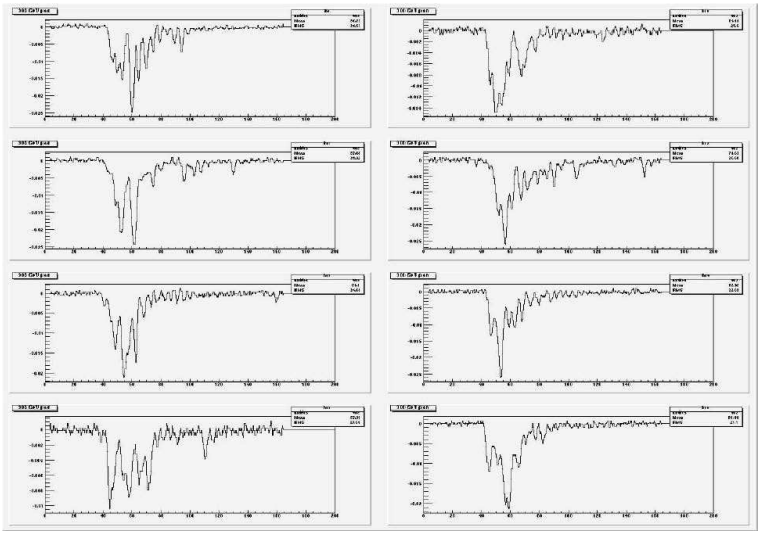

Fig. 31. Calorimeter pulses for eight individual events, voltage *vs.* time, observed with a photomultipler for minimum ionizing muons. The time scale is 0.4 ns per bin.

9.1 Muons

It is important to understand the response of HCAL to muons for not only overall calibration purposes, but also because a muon bit will be set in the trigger primitives for use in higher level event selection. The HCAL energy response to 225 GeV muons was measured by sending a 225 GeV muon beam into the center of each tower (see Fig. 32 which shows the response due to individual photoelectrons). Figure 35 shows single event displays for 225 GeV

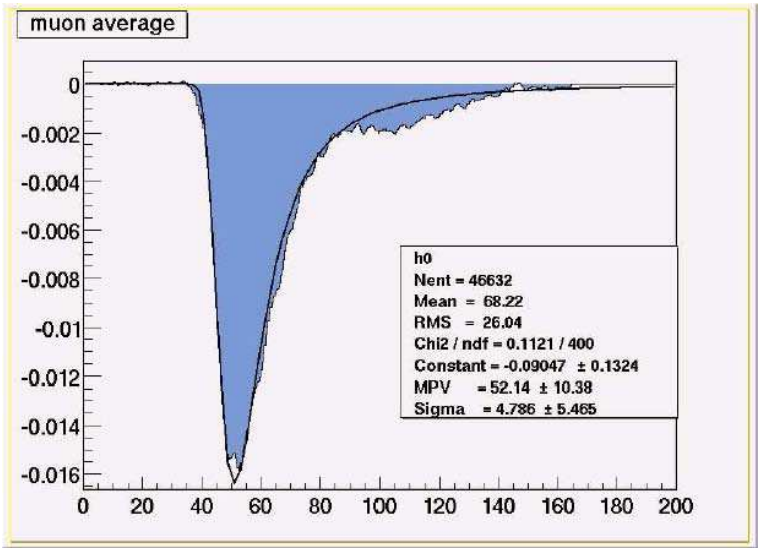

Fig. 32. Calorimeter pulses for 116 muon events added together, voltage *vs.* time, observed with a photomultipler. The time scale is 0.4 ns per bin.

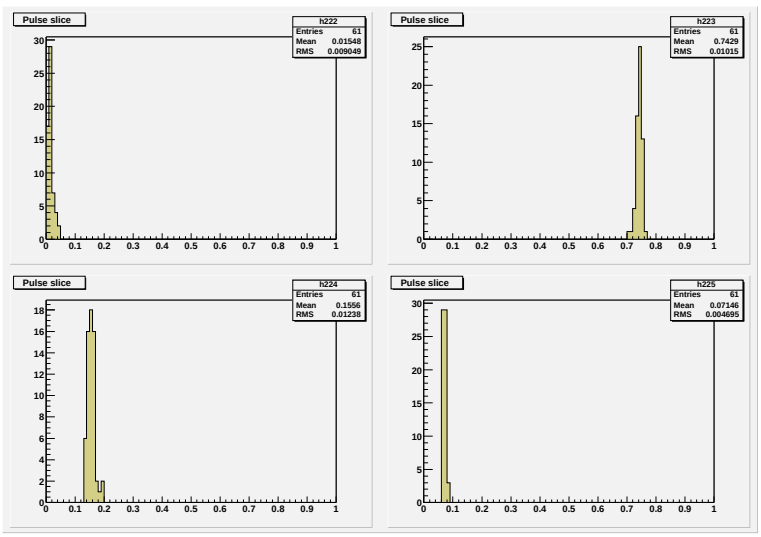

Fig. 33. Fraction of energy observed in 29.6 ns time bins for 200 GeV pion showers. a) first time bin, b) second time bin, c) third time bin and d) fourth time bin.

muons. The minimum-ionizing muon signal is clearly visible above the electronic noise, about 0.5 GeV, in neighboring towers. Figure 36 shows the energy response from a single tower that contains the muon. The fit value for the most probable response is 1.64 GeV.

9.2 Pions

Figure 37 shows single event displays for individual 300 GeV pions. Most of the energy is contained in the single tower on which the beam is centered.

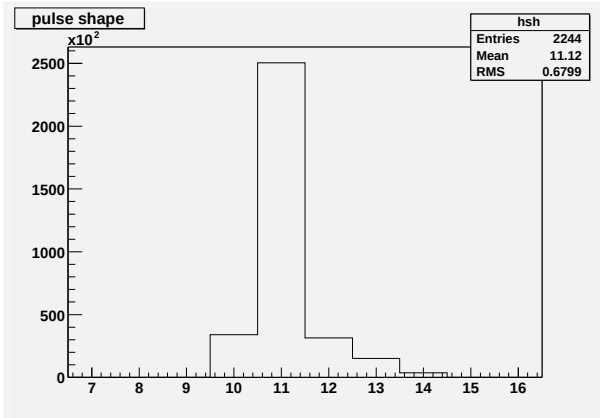

Fig. 34. Average pulse shape, energy (arb. scale) vs. time (29.6 ns bins) observed with a photomultiplier, when the fraction of energy in the first 29.6 ns time sample is selected to be of fixed value.

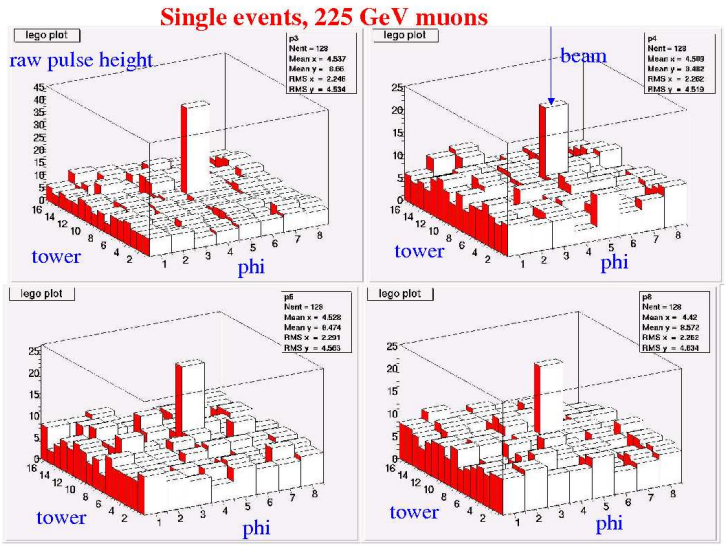

Fig. 35. Single 225 GeV muon events observed in the HB.

A 3×3 array of HCAL towers contains a large fraction of the energy of the energy from the hadronic shower.

The transverse containment of a hadronic shower in HCAL is illustrated in Fig. 38. With the beam centered on a tower, the fraction of energy observed in the single tower is about 75%. If the energy in the neighboring eight towers is added, forming a 3×3 array, about 93% of the pion energy is observed. The energy in a 5×5 array is about 96%.

The energy distribution observed in the 5×5 array for 100 GeV pions is shown in Fig. 39. The fitted Gaussian width of the distribution is about 9.7%.

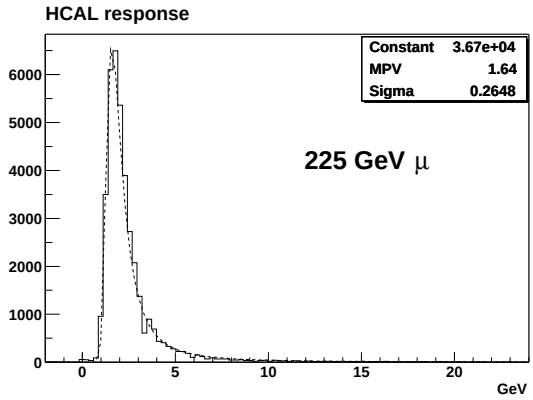

Fig. 36. Observed energy distribution in HCAL for minimum-ionizing muons. The most probable value is 1.64 GeV.

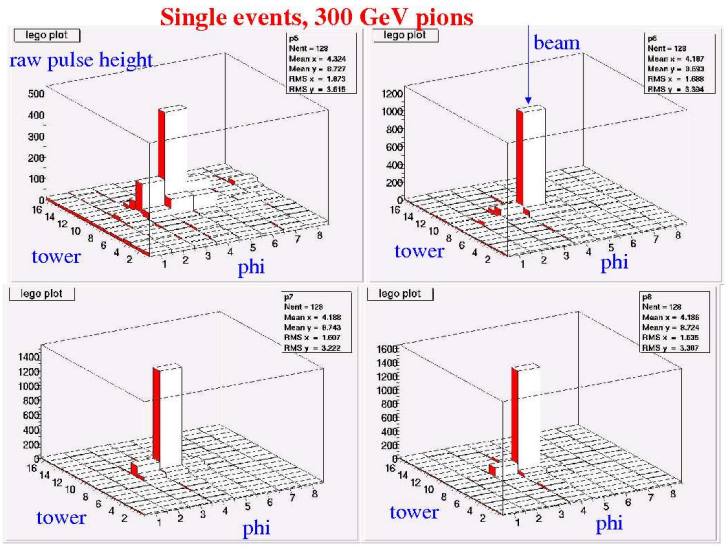

Fig. 37. Single 300 GeV pion events observed in the HB.

9.3 Electrons

Figure 40 shows single event displays for 100 GeV electrons sent directly into HCAL. While such showers cannot occur in CMS due to the presence of the ECAL crystals, these data nevertheless serve to document the response of HCAL to the electromagnetic shower component as well as to aid in the understanding of the overall calibration. As expected, all the energy is contained in the single tower on which the beam is centered.

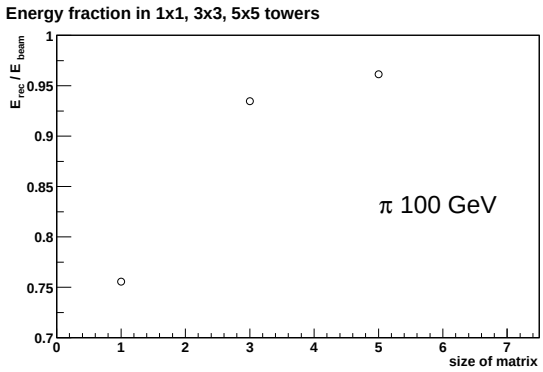

Fig. 38. Transverse containment of a 100 GeV pion shower, in terms of energy fraction observed in a single (1×1) tower, a (3×3) array of 9 towers and a (5×5) array of 25 towers. The beam is centered on the array.

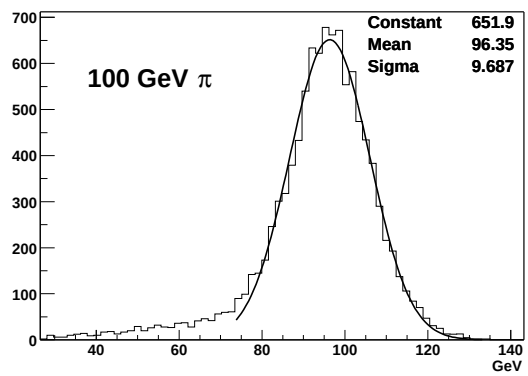

Fig. 39. Energy distribution in HCAL (5×5) for 100 GeV pions.

9.4 Cerenkov Studies

Light from the scintilators is tranmitted from the scintillating tiles to the readout boxes through optical fibers. These fibers are brought together in bundles at the boundary between phi slices at the $\eta = 16$ end of the wedges. When charged particles pass through the optical fibers, they may emit Cerenkov light with the potential to create a fake energetic signal. To investigate this effect, data were taken with a 300 GeV pion beam, positioned at $\eta = 16$ on the boundaries bewteen phi sectors, $\phi = 1.5$ and $\phi = 3.5$, respectively, corresponding to the regions of the fiber bundles. For purpose of this study, signals in two sets of channels were monitored, $\phi = 1$ and $\phi = 4$ with $1 < \eta < 7$. This set of channels was chosen so that any possible crosstalk in the HPDs would be negligible, even with no magnetic field present.

Figure 41 shows the energy in a single tower for $\phi = 1$ and $1 < \eta < 7$, for the case where the beam was located at either $\phi = 3.5$ or $\phi = 1.5$. There is a clear contribution of about 3 GeV to the tower energy when beam was positioned

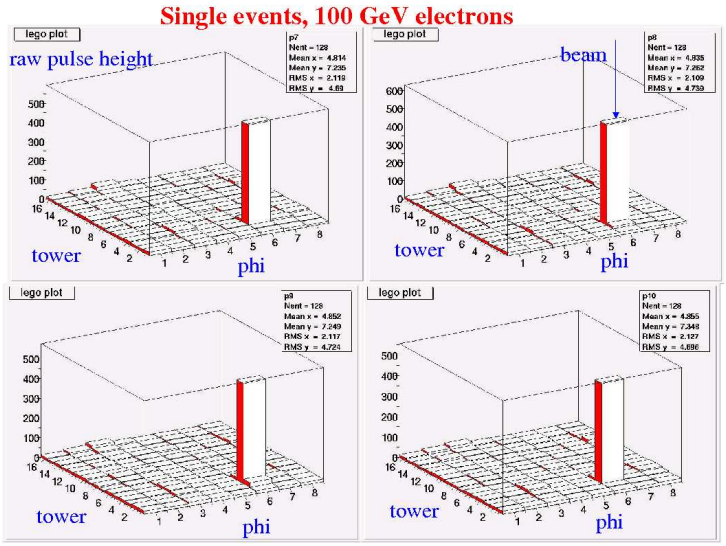

Fig. 40. Single 100 GeV electron events observed in the HB.

close to the phi sector boundary. Figure 42 shows the total energy summed over the eight η towers ($\phi = 1$), illustrating that signals due to Cerenkov light in the optical fibers appear in a single channel.

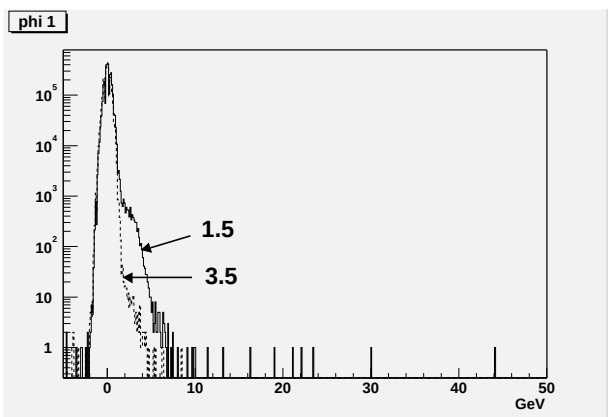

Fig. 41. Energy in a single tower for $\phi = 1$ when the beam is positioned at the adjacent phi sector boundary (1.5) or at a non-neighboring boundary (3.5). About 3 GeV of fake signal is observed to be caused by Cerenkov light in less than 1% of the events.

A few events out of the 4×10^5 taken have a measured energy greater than 10 GeV. For such an event, Fig. 43 shows the observed energy for 20 time samples in each of the 16 eta towers ($\phi = 1$). The Cerenkov signal appears at $\eta = 5$, while towers at $\eta = 1$ to 4 and 5 to 9 are consistent with electronics noise and the towers at $\eta = 12$ to 16 directly sample the beam. From this plot it is seen that the Cerenkov light is collected in a single time slice, a feature which will help us tag such events.

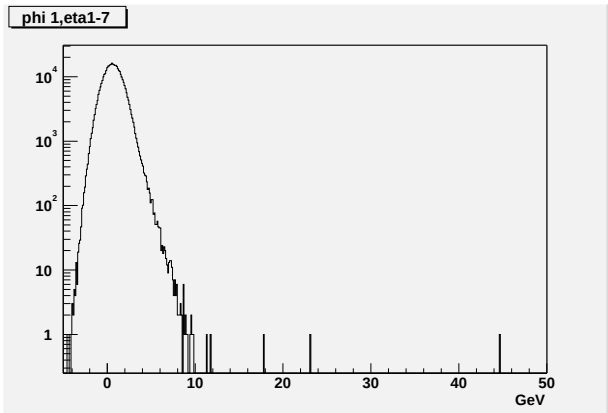

Fig. 42. Cerenkov signal summed over seven eta towers ($1 < \eta < 7$).

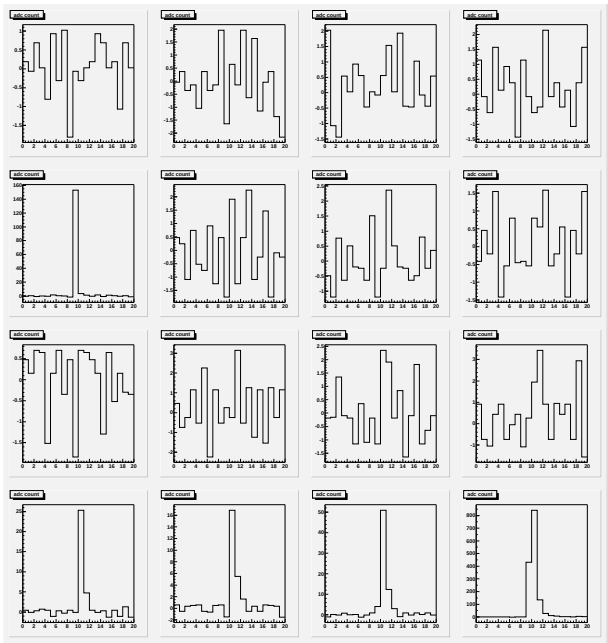

Fig. 43. Energy collected in 20 time samples for all 16 η towers.

10 Performance with Electromagnetic Crystals

In order to archive accurate calibration of the CMS hadron calorimeters, it is essential that the influence of the lead tungstate crystal electromagnetic calorimeter (ECAL) is fully understood and accounted for. A prototype ECAL module was placed on a support table which allowed positioning the crystals in the beamline, in front of any chosen HCAL tower, thus approximating the ECAL calorimeter that will be placed in front of HCAL in the CMS experiment.

The ECAL module was extensively calibrated with electron beams. There were two ECAL calibration periods, one at the end of June and the second during

August-September 2002. During the June run, a preliminary calibration of the electromagnetic calorimeter was made. The early runs were used to determine the apparatus functionality, in particular the performance of the charge to digital converter (QDC), and provided a preliminary calibration. Much of the analysis software was developed following this test beam period.

The high voltage of the photomultiplier tubes was adjusted to reduce gain variations of the individual channels. This allowed a relatively quick calibration of the ECAL during the second test beam period when the calibration of the hadron calorimeter wedges was the main point of interest. The second test beam period started in mid August 2002. The improvements of the data acquisition software and more precise data allowed for more accurate analysis of ECAL performance. The effects of changing temperature, radiation dose and electronics readout variations where monitored and evaluated. The final gains of the ECAL were determined so they could be used for combined ECAL+HCAL analysis. This resulted in a set of six epochs of separate sets of gains, covering the entire data set collected during 2002 HCAL testbeam.

Relative gains of 49 ECAL crystals were measured with 100 GeV electrons. Tests of the linearity of ECAL response was done with electron beams with energies 20, 30, 50, and 100 GeV. The calibration sets were divided into six epochs where either 7x7, 5x5 or 3x3 crystals where calibrated. The energy resolution of the ECAL module for 100 GeV electrons ranges between 1.6 GeV and 2.6 GeV. The non-linearity of the energy response to electrons between 20 and 100 GeV is 2%.

10.1 Crystal Calibration

In order to calibrate a given crystal, we made an attempt to center the beam on this particular crystal as much as possible. After the run was recorded, the data was analyzed to see if the beam was properly centered by looking at the left-right and up-down asymmetry of the energy deposited in the off-center crystals. Once the beam was properly centered on a crystal, 70%-80% of the electromagnetic shower was contained in a single targeted crystal.

We defined the gain (g_i) of a crystal as the coefficient that converts the energy (E_i) deposited in a crystal from QDC counts (Q_i) to GeV:

$$E_i = \frac{Q_i}{g_i}$$

Electromagnetic showers developing inside crystals are well contained (greater than 97% of the energy) in a 3x3 matrix of crystals centered around targeted crystal. Thus the energy (E) deposited by electrons in ECAL is defined as:

$$E = \sum_{i=1}^{9} E_i = \sum_{i=1}^{9} \frac{Q_i}{g_i}$$

Individual runs were dedicated to collecting the calibration data for each crystal, with 100 GeV/c electron beam centered on this particular crystal. The analysis was performed by iterating simultaneously all 49 crystal gains. The average event energy was then used to define new gains for each crystal:

$$g_j^{\text{new}} = \frac{<E_j>}{100} g_i^{\text{old}}$$

where j is the crystal index which runs from 1 to 49 and the average energy $< E_j >$ is determined from the data. Since raw QDC counts for 100 GeV/c electron run had typical values of 1000 counts, we set initial gain for all the crystals at 10.

The following three cuts were used to select sampled events:

- High and low energy cuts: 50GeV $< E_{\text{event}} <$ 150GeV,
- HCAL cut: $Q < 15$,
- f1 cut: $f_1 > 50\%$

10.2 ECAL linearity and resolution

All the calibration runs were made using 100 GeV electrons. To check the linearity of the ECAL energy response, data were taken with beam energies of 20, 30, 50 and 100 GeV. The response of a single crystal to the different energy elections is shown in Figs. 44.

Fig. 45 shows the linearity of the energy response and the fractional resolution derived from Gaussian fits to the energy distributions. For the lower energies, the mean/energy tends to be greater than one, whereas for the beam energy of 100 GeV, the mean/energy is smaller than one. This is because at lower energies less of the electromagnetic shower can leak out the back.

The calibration of the full 7×7 matrix of lead tungstate crystals was performed using a 100 GeV electron beam. The energy resolution at 100 GeV varied from 1.6 to 2.6 GeV for several data sets. The observed non-linearity of electron energy response between 20 and 100 GeV is 2%. Clearly the performance of this ECAL module is worse the final CMS design [13]; however, the ECAL resolution is satisfactory from point of view of the goals of the 2002 HCAL test beam data taking. The electronic noise for the sum of 3×3 crystals averages around 0.7GeV.

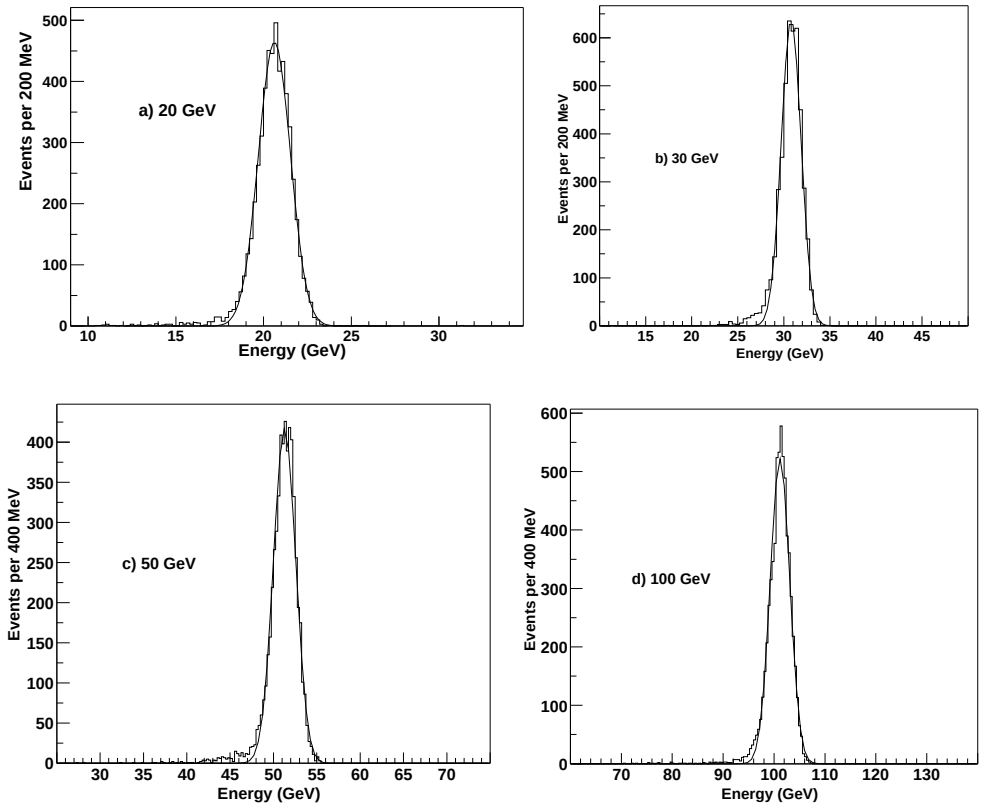

Fig. 44. Single crystal response to electrons of energy a) 20 GeV, b) 30 GeV, c) 50 GeV, and d) 100 GeV.

10.3 ECAL and HCAL combined performance

The response of the ECAL plus HCAL system was studied with pion beams of varying momenta. These pion beams had a contamination due to muons and electrons which was generally worse at lower momenta. A plot of HCAL *vs.* ECAL is shown in Fig. 46 for pions of momenta 30 GeV/c. The data show the expected contributions from pions and muons. Also present is a band of events with zero HCAL energy and an ECAL energy less than 30 GeV. These events were due to electrons in the beam. Fig. 46 (right) shows a histogram of the total measured energy (ECAL plus HCAL). The pion and muon peaks are clear, while the previously mentioned beam contamination affects the lower energy tail of the pion peak. Figure 47-49 show the same plots for 50, 100, and 300 GeV/c pions. At 50 GeV, the beam contamination is less severe than at 30 GeV, while at 100 and 300 GeV the beams are relatively clean.

The absolute energy scale of the HB was defined using a beam of 50 GeV pions directed to the ECAL plus HCAL configuration. Only those pions which

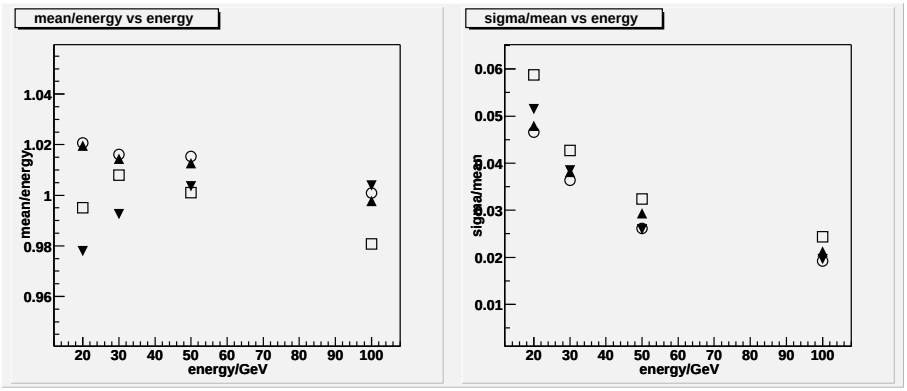

Fig. 45. Left: Mean energy divided by beam energy vs. beam energy. Right: sigma divided by mean energy vs. beam energy. The points correspond to diffeent data runs over time where the beam was centered on the central crystal in the 7×7 matrix. The spread of the data indicates the systematic error levels. The statistical errors are smaller than the size of the symbols.

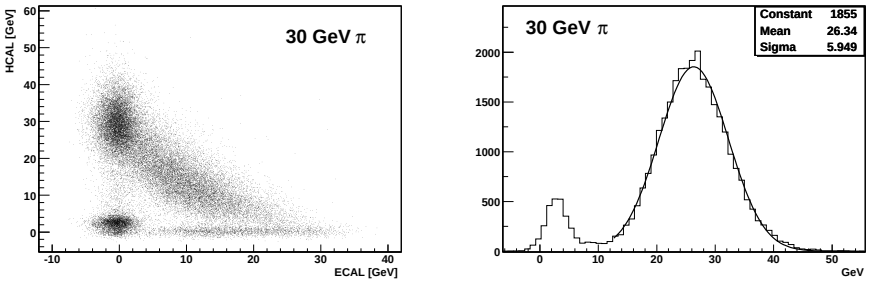

Fig. 46. left: Energy observed in HCAL *vs.* ECAL for 30 GeV pions. Right: Total energy, ECAL plus HCAL.

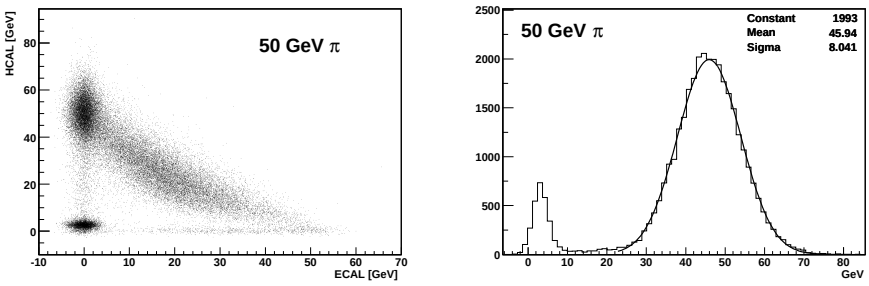

Fig. 47. left: Energy observed in HCAL *vs.* ECAL for 50 GeV pions. Right: Total energy, ECAL plus HCAL.

deposited less than 2 GeV in the crystals were selected. The calibration factor was extracted from the ratio between the initial pion energy and the mean of the distribution of summed energy deposited in a 5×5 tower matrix centered on the target tower.

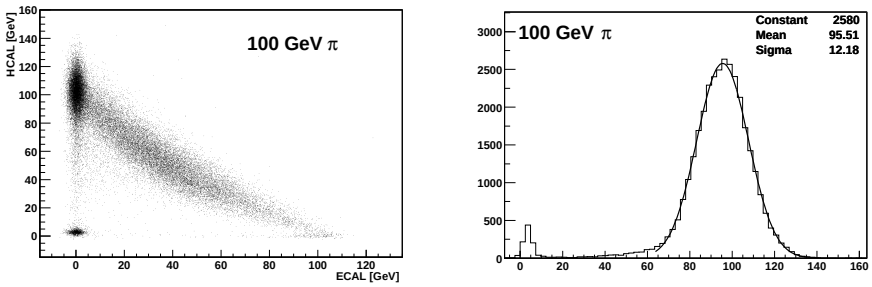

Fig. 48. left: Energy observed in HCAL *vs.* ECAL for 100 GeV pions. Right: Total energy, ECAL plus HCAL.

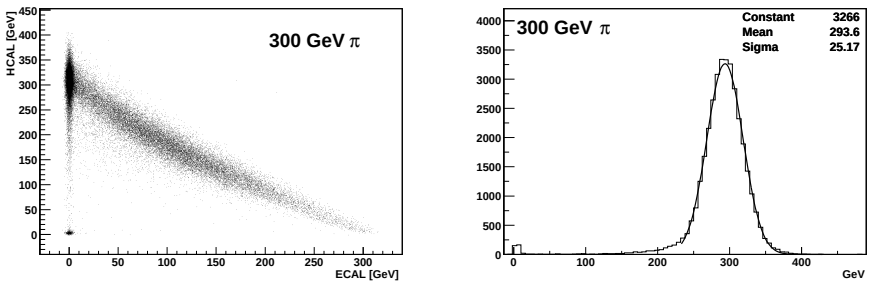

Fig. 49. left: Energy observed in HCAL *vs.* ECAL for 300 GeV pions. Right: Total energy, ECAL plus HCAL.

10.4 Resolution and linearity

The energy resolution and the linearity of the energy dependence of the response to pions are two typical quantities used to characterize the performance of a hadronic calorimeter.

10.4.1 Energy distributions for pions

At 50 GeV and below, the pion beam contained a significant contamination. Since this contamination can effect on the resolution and linearity at low energy, a series of cuts were developed to clean up the beam.

Figure 50 shows the HCAL *vs.* ECAL energy for the worst case encountered, that of 20 GeV pions. To clean up the beam, cuts were made in the HCAL-ECAL energy plane. The Geant4 [21] Monte Carlo program was then used to correct for these cuts. A "horizontal" cut of $E_{\mathrm{H}} > 6.5$ GeV, where E_{H} is the HCAl energy, was made in order to eliminate the events with abnormally small HCAL energy. Since this cut then biased the Gaussian peak due to muons, an additional "diagonal" cut of $E_{\mathrm{H}} > -0.83E_{\mathrm{E}} + 5.2$ GeV, where E_{E} is the ECAL energy, was made. The corresponding cuts for other beam energies are summaried in Table 4. After applying the cuts, the distributions of ECAL plus

HCAL energy were fit to Gaussian distributions.

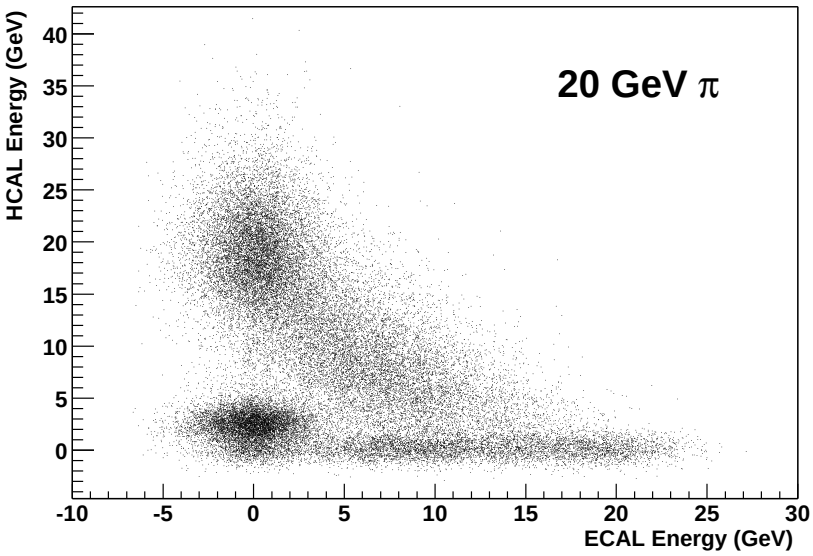

Fig. 50. Energy observed in HCAL *vs.* for 20 GeV pions.

The energy response and fractional energy resolution was determined as a function of the pion beam energy from both the standard deviation and mean of the nominal distributions, as well as from the corresponding Gaussian fits. The energy response was calculated as $\bar{E}/E_\pi$, where $\bar{E}$ is the mean of the Gaussian fit to the energy distribution and E_π is the energy of the pion beam. The resolution was calculated as the rms (σ) of the energy distribution. These response and resolution measurements were corrected for the effect of the beam cuts, using a Monte Carlo simulation based on Geant4. Beams of pions were generated and showered through a detailed simulation of the ECAL plus HCAL test beam setup, and the resulting distributions were scaled up to match the mean energy of the associated data distributions. Then, the quality cuts for background rejection were applied and correction factors were derived and applied to the data. The correction factors to response and resolution for 20 GeV (30 GeV) pions are 0.931 (0.987) and 1.056 (1.018), respectively. Corrections for pions with 50 GeV or higher energy are negligible.

Table 4. Cuts used to clean up the low energy pion beams.

There are three contributions to the HCAL calibration error. One comes from the 2 GeV cut to the ECAL energy deposition by 50 GeV pions, and was estimated to be about 1% by varying this cut between 0 and 3 GeV. The second contribution, 0.5%, comes from the background subtraction method applied to the 50 GeV calibration sample. The third component of the calibration uncertainty, 0.1%, is the statistical error on the mean of the 50 GeV distribution.

energy	*horizontal cut*	*diagonal cut*
20	$E_{\mathrm{H}} > 6.5$ GeV	$E_{\mathrm{H}} > -0.83E_{\mathrm{E}} + 5.2$ GeV
30	$E_{\mathrm{H}} > 6.5$ GeV	$E_{\mathrm{H}} > -1.2E_{\mathrm{E}} + 10.7$ GeV
50	$E_{\mathrm{H}} > 6.5$ GeV	$E_{\mathrm{H}} > -1.0E_{\mathrm{E}} + 12.8$ GeV
100	$E_{\mathrm{H}} > 6.5$ GeV	$E_{\mathrm{H}} > -1.0E_{\mathrm{E}} + 12.8$ GeV
300	$E_{\mathrm{H}} > 6.5$ GeV	$E_{\mathrm{H}} > -1.0E_{\mathrm{E}} + 12.8$ GeV

Added in quadrature, the total calibration uncertainty is ± 0.013. This error on the pion energy was propagated to the mean and width of the distributions by recalculating the total energy with the nominal, high, and low calibration factors.

Table 5 shows the results of the fits to the total ECAL plus HCAL energy response to pions. Figure 51 shows the fit resolution as a function of pion energy, and Fig. 52 shows the resulting linearity. The vertical bars are the statistical and systematic uncertainties in the data measurement added in quadrature. The comparison with Geant4 is discussed in the next section.

10.5 Comparison with Geant4

The CMS Collaboration developed the Object oriented Simulation for Cms Analysis and Reconstruction (OSCAR) framework [22], based on the Geant4 tool kit, to describe the detector geometry and the passage of particles through the detector material. Geant4 uses either parametric (LHEP) or microscopic (QGSP) physics models to simulate the particle showers arising from the interaction of particles with matter. For the studies presented in this note, the software package OSCAR 2.4.5 is used, based on GEANT 4.5.2, with LHEP 3.6 and QGSP 2.7 physics lists or models.

Table 5. Results of the fits to ECAL plus HCAL response to pions.

E_{b} (GeV)	$\bar{E}$ GeV	σ	$\sigma/\bar{E}$	Stat. err.	Bkgnd. err.	Calib. err.
20	18.3	4.6	27.1	0.15	5	0.1
30	28.9	5.8	27.1	0.12	3	0.2
50	46.2	8.0	27.1	0.10	0.6	0.2
100	96.0	12.4	27.1	0.07	0.4	0.3
300	295	4.6	25.2	0.05	0.0	0.3

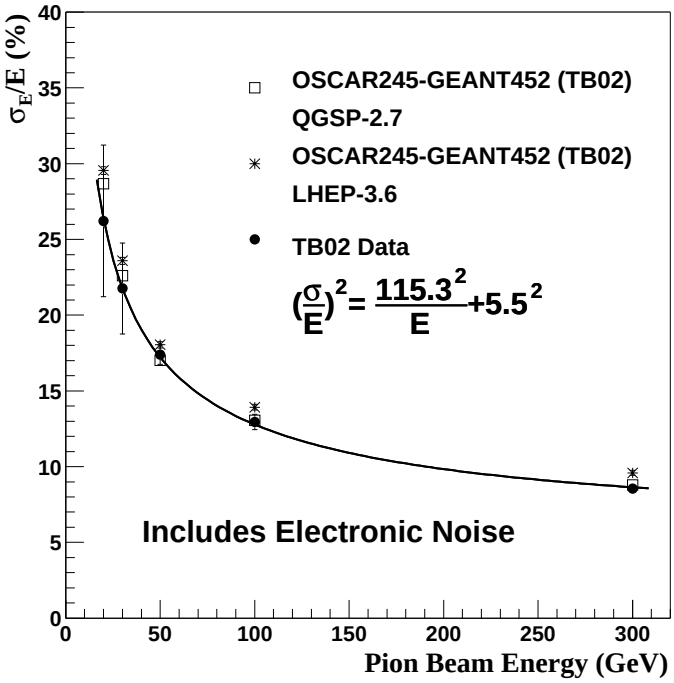

Fig. 51. Measured energy resolution (solid circles) with fit (line) compared to two different tunes of Geant4 (open squares and stars).

10.5.1 Geometry

The geometry of the Test Beam 2002 HCAL setup was divided into four units: the beam line (BL), the ECAL module, the HB wedge, and the HO. Originally, the geometry code was developed using GEANT4 classes under OSCAR 1.4.0 (and older versions). This geometry was later translated to XML format to comply with the OSCAR 2 requirements.

By default, the BL and the ECAL subsystems are aligned along the x direction. The HB wedges are also placed along the x direction with the inner face next to the end of the ECAL and the outer face followed by the HO. Figure 53 illustrates the calorimetry geometry. The ECAL module may be translated and rotated to point to a particular HB tower. The BL must also translate and rotate to follow a change in the test beam direction. The HB and the HO are fixed in space.

A detailed comparison using Geant4 was made for the tower no. $(\eta, \phi) = (9, 4)$. The electronic noise was taken to be 520 MeV in the Monte Carlo, in accordance with the pedestal measurement and the energy calibration scale. Production cuts in range for secondary particles are Geant4 user defined parameters which control the shower development. These cuts were set to 1 mm

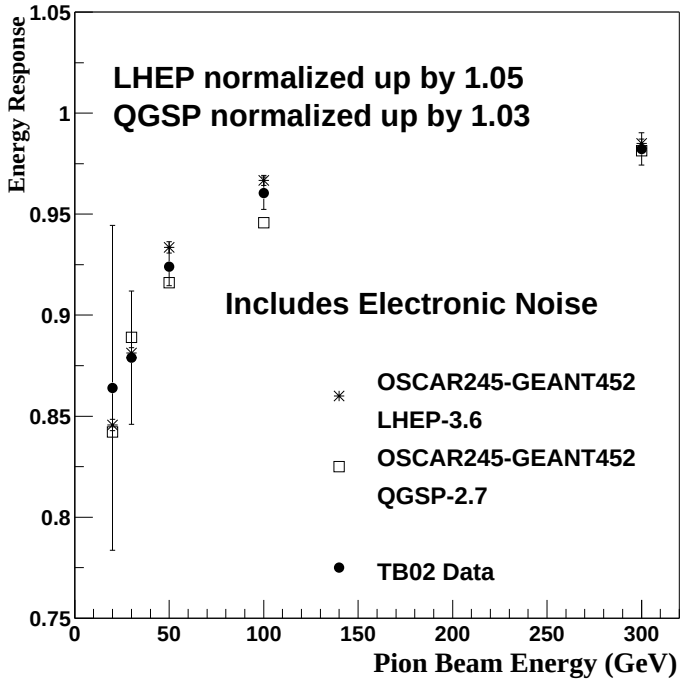

Fig. 52. Measured linearity compared to Geant4 simulations.

for both electrons and positrons and 10 mm for photons, except in the ECAL where the later cut was set to 1 mm. Figure 54 shows a simulated interaction of a 100 GeV pion.

10.5.2 Monte Carlo calibration

The energy calibration of the ECAL box and the HB in the simulation follows closely the same procedure used with the data. For 100 electrons in ECAL, the two Geant4 physics lists, LHEP-3.6 and QGSP-2.7, give energy resolutions in excellent agreement with each other (Fig. 55. For the ECAL module, an additional random term was tuned so that the electron energy resolution simulated in the range 20-100 GeV agreed with the experimental values: 5% (20 GeV), 3% (50 GeV), and 2.2% (100 GeV). The relative degradation in the fractional energy resolution for pions when incorporating the extra smearing into the ECAL energy is 3% (1% absolute) at 20 GeV, and 0.6% (0.06% absolute) at 300 GeV.

The energy distributions for 50 GeV pions, using the LHEP-3.6 and QGSP-2.7 physics lists, are displayed in Fig. 56.

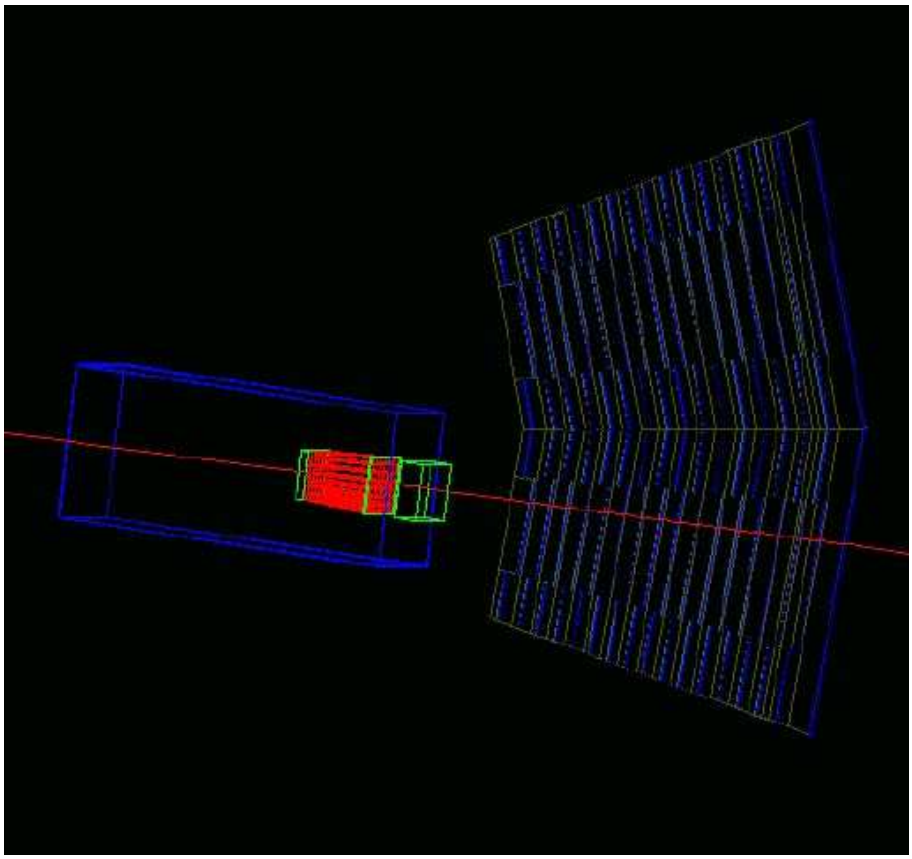

Fig. 53. Geometry of the calorimetry as coded into Geant4.

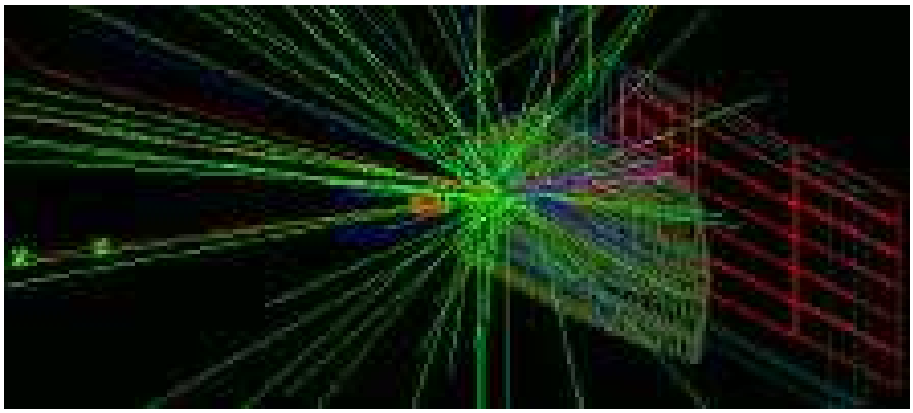

Fig. 54. Fully simulated interaction of a 100 GeV using Geant4.

10.5.3 Simulation results

The energy resolution of ECAL plus HCAL was shown in Fig. 51. The vertical bars are the statistical and systematic uncertainties in the data measurement added in quadrature. The data measurement is in good agreement with the simulation, for the two physics lists tested, given the high correlation of the

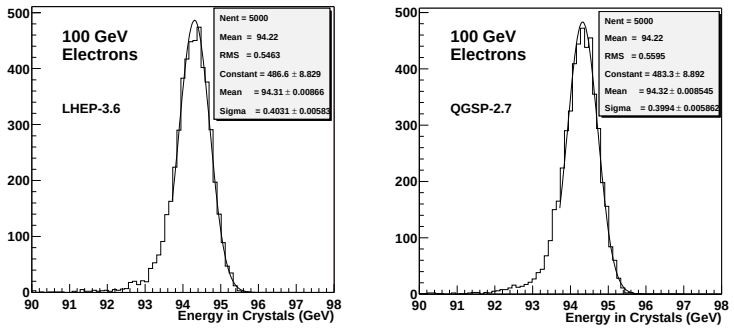

Fig. 55. Monte Carlo energy distribution in the crystals for 100 GeV electrons. Left: Physics list LHEP-3.6. Right: Physics list QGSP-2.7.

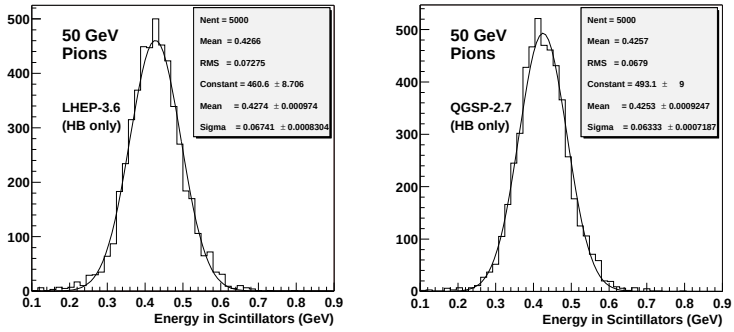

Fig. 56. Monte Carlo energy distribution in the scintillators for 50 GeV pions. Left: Physics list LHEP-3.6. Right: Physics list QGSP-2.7.

data uncertainties point-to-point in pion energy. The LHEP-3.6 physics list gives a fractional energy resolution a few percent larger than the QGSP-2.7 list. The data results and Monte Carlo prediction are easier to compare in the ratio plot shown in Fig. 57. The importance of the electronic noise contribution increases as the pion beam energy decreases. At 20 GeV, the resolution degrades by a little more than 30% when a realistic electronic noise model for our test apparatus is incorporated to the simulation.

The result from the simulation, using LHEP-3.6 or QGSP-2.7, including electronic noise, is compared with the linearity data in Fig. 52. The vertical bars are the statistical and systematic uncertainties in the data measurement added in quadrature. For comparison, the simulated linearity plots were scaled up by 5% (LHEP) and 3% (QGSP) to approximately match the data at 300 GeV. Within the experimental uncertainties, there is good agreement between the data and the simulation. While the LHEP-3.6 physics list predicts a response growing slightly faster with energy than measured, the one derived from the QGSP-2.7 physics list grows slower. The electronic noise does not affect this measurement significantly. The data measurement and the simulation are eas-

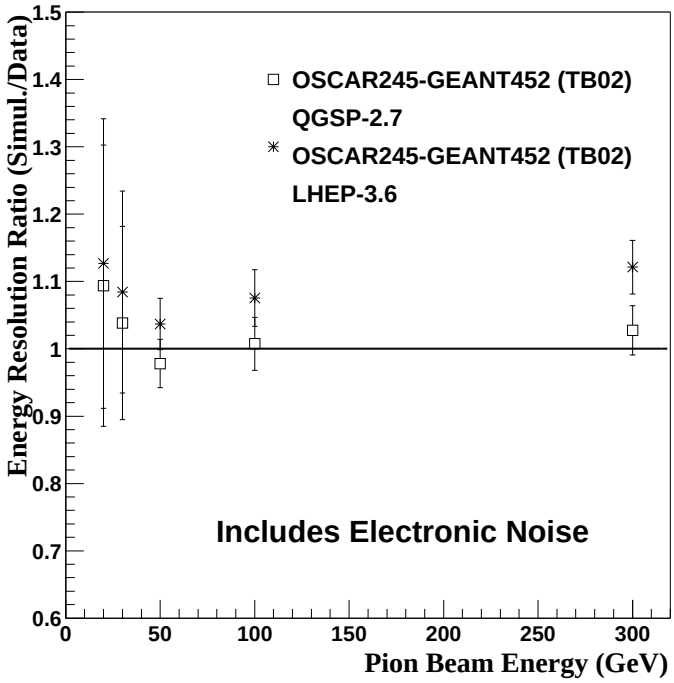

Fig. 57. Measured energy resolution (solid circles) with fit (line) compared to two different tunes of Geant4 (open squares and stars).

ier to compare in Fig. 58, which shows the ratio between the results from the simulation and the data.

11 Radioactive Source Calibration

The response of each scintillator of HB to a moving radioactive source was measured. This system will be used to carry the calibration found using electron and pion beams to HCAL towers not expposed to these beams.

The length of the optical fibers between the scintilators and the photo detectors varies with η. The source calibration data were used to measure and verify the tower-by-tower attenuation as a test of the technique. Figure 64 shows the relative response to the source of as a function of η for several ϕ slices. These data show that the light yield at the HPD is about 30% lower at $\eta = 1$ in comparison to $\eta = 14$. (The $\eta = 15$ and 16 towers are not included in these measurements because they are segmented longitudinally.) The effective attenuation length may be estimated according to the expression

$$E_{14} = E_1 e^{-d/L} \ ,$$

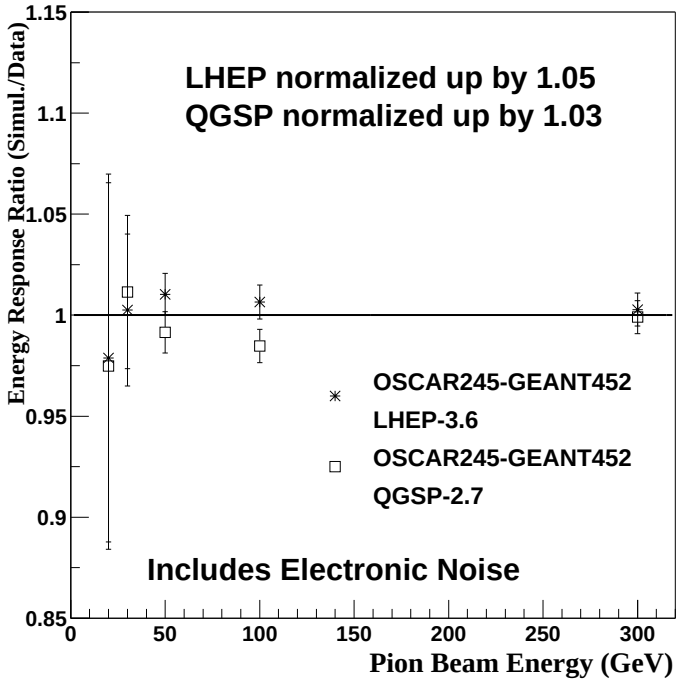

Fig. 58. Measured linearity compared to Geant4 simulations.

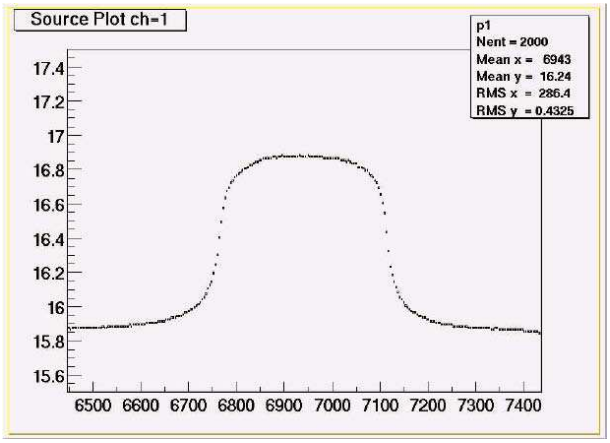

Fig. 59. Response of a scintillating tile as the radioactive source passes by it.

where E_{14} and E_1 are the measured response for towers 14 and 1 respectively, $d = 3.4$ m is the distance between centers of towers 14 and 1, and L is the attenuation length. The data are consistent with a value of L approximately equal to 10 m.

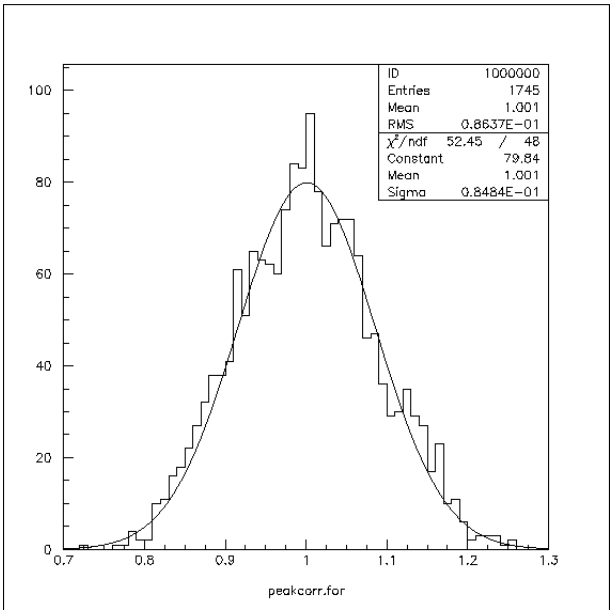

Fig. 60. Distribution of scintillating tile response to the source calibration. The observed rms spread of about 8% is consistent with that observed by source measurements taken during tile assembly.

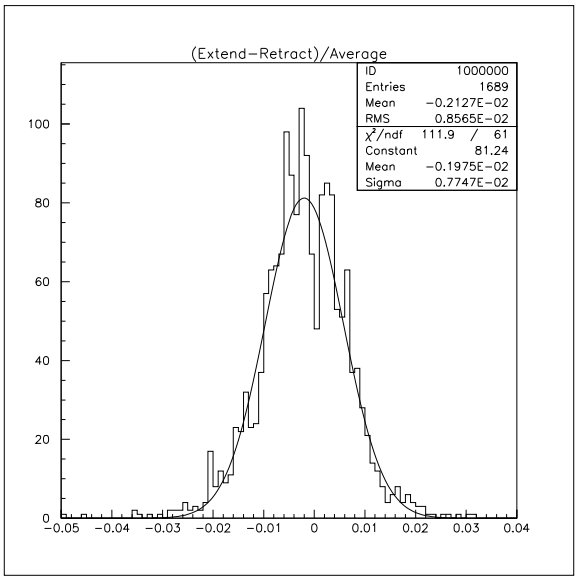

Fig. 61. Difference in peak response when the radiative source is extending or retracting.

12 Acknowledgments

References

[1] "CMS Technical Proposal," CERN/LHCC 94-38, LHCC/P1 (December 1994).

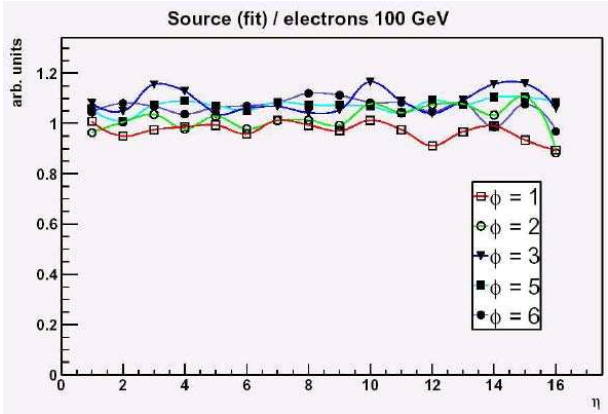

Fig. 62. Ratio of radioactive source signal to electron signal.

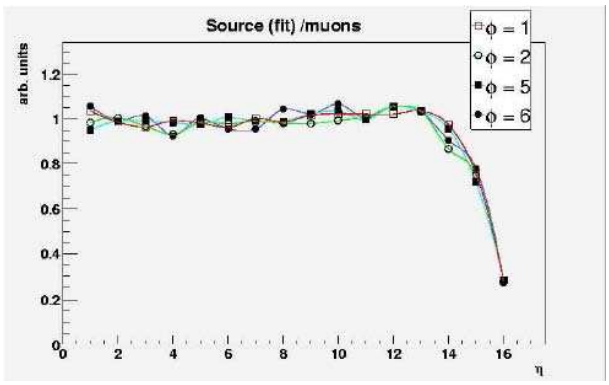

Fig. 63. Ratio of radioactive source signal to muon signal.

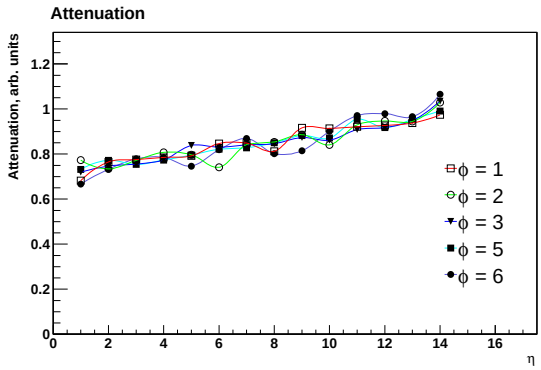

Fig. 64. Measurement of the attenuation *vs.* tower number (η). The attenuation occurs in the propagation of the signals in clear fibers from the towers to the readout box which is located on the $\eta = 16$ end of the wedge.

[2] The LHC design report and current status is available at http://lhc-new-homepage.web.cern.ch/lhc-new-homepage/ .

[3] "CMS, The Hadron Calorimeter Technical Design Report," CERN/LHCC 97-31 CMS TDR 2 (June 1997).

[4] CMS, The TriDAS Project, Technical Design Report, Volume 1: The Trigger Systems, CERN/LHCC 2000 - 38, CMS TDR 6.1, 599 pages, December 15, 2000.

[5] CMS, The TriDAS Project, Technical Design Report, Volume 2: Data Acquisition and High-Level Trigger, CERN/LHCC in press, 530 pages, December 2002.

[6] The HCAL/JetMET offline activities are described at http://www.uscms.org/scpac/JetMet/ .

[7] M.G. Albrow *et al.*, Nucl. Instr. Meth. A 256 (1987) 23.

[8] V.I. Kryshkin and A.I. Ronzhin, Nucl. Instr. Meth. A 247 (1986) 583.

[9] G.W. Foster, J.Freeman, and R.Hagstrom, Nucl. Phys. B23 (1991) 93; P. de Barbaro et al., Nucl. Instr. Meth. A 315 (1992) 317.

[10] CMS HCAL Collaboration, "Synchronization and Timing in the CMS Hadron Calorimeter," "Design, Performance, and Calibration of CMS Hadron-Endcap Calorimeter Wedges," "Design, Performance, and Calibration of CMS Forward Calorimeter Wedges," "Longitudinal Shower Profiles Measured in CMS HCAL and Comparison with Geant4," papers in preparation.

[11] V. V. Abramov *et al.* [CMS-HCAL Collaboration], "Studies of the Response of the Prototype CMS Hadron Calorimeter, Including Magnetic Field Effects, to Pion, Electron, and Muon Beams," Nucl. Instr. and Meth. A 457 (2001) 75.

[12] E. Hazen *et al.*, "Radioactive Source Calibration Technique for the CMS Hadron Calorimeter," Nucl. Instr. and Meth. A 511 (2003) 311.

[13] "CMS, The Electromagnetic Calorimeter Technical Design Report," CERN/LHCC 97-33, CMS TDR 4 (Dec. 1997).

[14] P. Cushman, A. Heering, and A. Ronzhin, "Custom HPD Readout for the CMS HCAL," Nucl. Instr. and Meth., A 442 (2000) 289.

[15] T. Zimmerman and M. Sarraj, "A Second Generation Charge Integrator and Encoder ASIC," IEEE Trans. Nucl. Sci. NS-43 (1996) 1683.

[16] T. Zimmerman and J. R. Hoff, "The Design of a Charge-Integrating Modified Floating-Point ACD Chip," IEEE J. Solid-State Circuits 39 (2004) 895.

[17] The Channel Link is described in the National Semiconductor data sheet, "DS90CR285/DS90CR286, +3.3V Rising Edge Data Strobe LVDS 28-Bit Channel Link-66 MHz," (November 2000).

[18] E. Hazen, J. Rohlf, S. Wu, A. Baden, and T. Grassi, "The CMS HCAL Data Concentrator: A Modular, Standards-Based Implementation," Proceedings of the 7th Workshop on Electronics for LHC Experiments, Stockholm, CERN 2001-005 and CERN/LHCC/2001-034, 347 (2001).

[19] H.C. van der Bij, O. Boyle, and R. A. McLaren, "S-LINK, a Data Link Interface Specification for the LHC Era", Proceedings of the Beaune 97 Xth IEEE Real Time Conference (1997).

[20] G. Davies, J.-P. Peigneux, A. Signovski, and C. Seez, "A Study of the Monitoring of Radiation Damage to CMS ECAL Crystals, Performed at X5-GIF," J. Phy. G: Nucl. Part. Phys. 26 (2000) 1735.

[21] S. Agostinelli *et al.*, "Geant4: a simulation toolkit," Nucl. Inst. Meth. **A506** (2003) 250; http://wwwasd.web.cern.ch/wwwasd/geant4/geant4.html .

[22] For CMS, the Geant4 simulation is incorporated into a package called Object oriented Simulation for CMS Analysis and Reconstruction (OSCAR), http://cmsdoc.cern.ch/oscar.